Supporting Information

Assembly of Mn^{III} ions into Di-, Tetra-, Deca-nuclear Coordination Complexes, Zero- to Three-Dimensional Molecular Framework: Molecular Spin Flop to and short Range Bulk Magnetic Spin Flop Ordering

Jayasree Kumar, [a] Ibtesham Tarannum,[b] Yan-Zhen Zheng,[c*] Saurabh Kumar Singh,[b*] Kartik Chandra Mondal[a*]

[a]Department of Chemistry, Indian Institute of Technology Madras, Chennai, India

[b]Department of Chemistry, Indian Institute of Technology Hyderabad, Kandi, Sangareddy, Telangana, India-502285

[c]Frontier Institute of Science and Technology, Xi'an Jiaotong University, 99 Yanxiang Road, Xi'an, Shaanxi 710054, P. R. China.

Contents:

1. Crystallographic Information

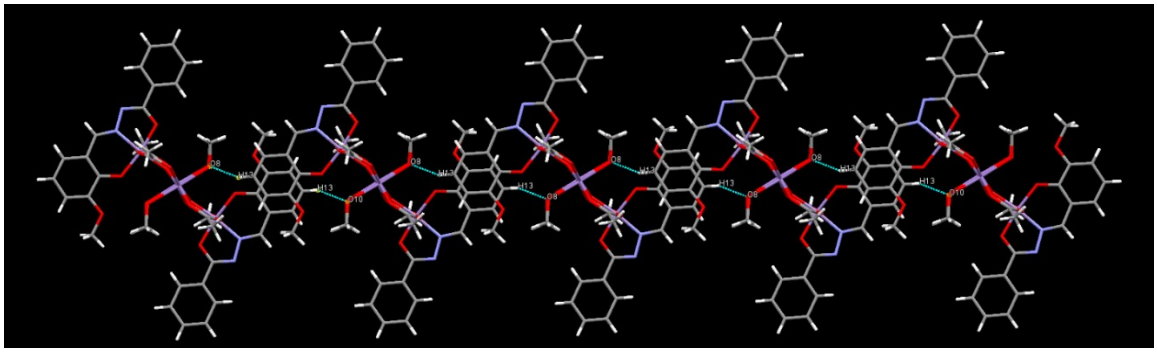

Figure S1. H-bonding interactions (O8---H13-C) in Mn^{III}_4 of $[Mn^{III}_4(\mu_3\text{-}O)_2(L^1)_2(OAc)_4(HOMe)_4]$ (**1**).

Table S1. Crystal structural refinement data parameters of complexes **1**, **2**, **3** and **4**.

Complex	1	2	3	4
Chemical formula	$C_{42}H_{48}Mn_4N_4O_{20}$	$C_{30}H_{34}Mn_2N_6O_8$	$C_{30}H_{28}Mn_2N_6O_8$	$C_{136}H_{118}Mn_{10}N_{24}O_{42}S_{10}$
Formula weight	1148.60	716.51	710.46	3081.19
CCDC Number	1860848	1860849	1860850	2180490
Crystal size (mm)	0.250 x 0.220 x 0.100	0.150 x 0.100 x 0.100	0.200 x 0.150 x 0.150	0.11 × 0.34 × 0.11
Crystal system	Triclinic	Triclinic	Triclinic	Triclinic
Space group	$P\bar{1}$	$P\bar{1}$	$P\bar{1}$	$P\bar{1}$
***a* (Å)**	10.5827(6)	7.8214(5)	10.063(12)	9.888 (4)
***b* (Å)**	11.1323(7)	9.9952(6)	12.143(15)	20.717 (9)
***c* (Å)**	12.6983(8)	10.4841(7)	15.195(17)	21.011 (9)
***α* (deg)**	104.061(3)	94.868(2)	68.52(4)	71.075 (7)
***β* (deg)**	113.978(3)	105.897(2)	73.73(4)	77.324 (8)
***γ* (deg)**	90.275(3)	94.543(2)	71.10(6)	80.532 (7)
***V* (Å^3)**	1316.85(14)	780.92(9)	1607(3)	3952 (3)
Z	1	1	2	1
***T* (K)**	200(2)	200(2)	200(2)	100(2)
***λ* (Å)**	0.71073	0.71073	0.71073	0.71073
D_{calc} (g cm^{-3})	1.448	1.524	1.468	1.627
***μ* (mm^{-1})**	1.012	0.869	0.844	0.99
***R*$_{int}$**	0.0575	0.0670	0.0560	0.047
***R*$_1$ [I > 2*σ*(I)]^a**	0.0512	0.0472	0.0684	0.092
w*R*$_2$ (all data)^b	0.1236	0.1252	0.1855	0.294
Total reflections	10286	23839	53693	41097
Independent reflections	4190	2742	7649	1806
Reflections ; *I*> 2σ(*I*)	5274	12618	5494	15457
Δρ$_{max}$ (e Å^{-3})	+ 1.733	+ 1.974 e Å^{-3}	1.549	3.54
Δρ$_{min}$ (e Å^{-3})	−0.469	−1.134	-1.284	-1.44

GooF	0.820	1.166	1.1068	1.11

$[Mn^{III}_4(\mu_3\text{-}O)_2(L^1)_2(OAc)_4(HOMe)_4]$ (**1**)

$[Mn_2(L^2)_2(\mu\text{-}OMe)_2(HOMe)_2]$ (**2**)

$[Mn(L^3)(OMe)]_n$ (**3**)

$[Mn_{10}(L^4)_8(OL^4)_2(DMF)_4(MeOH)_4(H_2O)_2]$ (**4**)

Selected bond lengths and bond angles

Table S2. Selected bond lengths [Å] and angles [°] of $[Mn^{III}_4(\mu_3\text{-}O)_2(L^1)_2(OAc)_4(HOMe)_4]$ (**1**).

Mn(1)-O(6)	1.893(3)
Mn(1)-O(1)	1.927(3)
Mn(1)-O(2)	1.925(3)
Mn(1)-N(1)	1.973(4)
Mn(1)-O(4)	2.172(4)
Mn(1)-O(3)	2.178(4)
Mn(2)-O(6)#1	1.891(3)
Mn(2)-O(6)	1.897(3)
Mn(2)-O(9)#1	1.957(3)
Mn(2)-O(7)	1.959(4)
Mn(2)-O(8)	2.235(3)
Mn(2)-O(10)	2.257(3)
Mn(2)-Mn(2)#1	2.8815(15)
O(6)-Mn(1)-O(1)	94.91(13)
O(6)-Mn(1)-O(2)	93.39(13)
O(1)-Mn(1)-O(2)	171.69(14)
O(6)-Mn(1)-N(1)	173.01(14)
O(1)-Mn(1)-N(1)	92.05(14)
O(2)-Mn(1)-N(1)	79.65(14)
O(6)-Mn(1)-O(4)	95.23(13)
O(1)-Mn(1)-O(4)	87.43(14)
O(2)-Mn(1)-O(4)	91.65(14)
N(1)-Mn(1)-O(4)	84.43(15)
O(6)-Mn(1)-O(3)	95.14(13)
O(1)-Mn(1)-O(3)	86.91(13)
O(2)-Mn(1)-O(3)	92.52(14)
N(1)-Mn(1)-O(3)	85.85(15)
O(4)-Mn(1)-O(3)	168.57(13)
O(6)#1-Mn(2)-O(6)	80.95(14)
O(6)#1-Mn(2)-O(9)#1	97.55(15)
O(6)-Mn(2)-O(9)#1	174.44(14)
O(6)#1-Mn(2)-O(7)	173.01(15)
O(6)-Mn(2)-O(7)	97.17(15)

O(9)#1-Mn(2)-O(7)	84.94(16)
O(6)#1-Mn(2)-O(8)	96.03(14)
O(6)-Mn(2)-O(8)	90.58(12)
O(9)#1-Mn(2)-O(8)	84.24(14)
O(7)-Mn(2)-O(8)	90.72(15)
O(6)#1-Mn(2)-O(10)	89.02(13)
O(6)-Mn(2)-O(10)	97.45(13)
O(9)#1-Mn(2)-O(10)	87.86(14)
O(7)-Mn(2)-O(10)	84.54(14)
O(8)-Mn(2)-O(10)	171.12(13)

Symmetry transformations used to generate equivalent atoms:

#1 -x+1,-y+2,-z+1

Table S3.1. Selected bond lengths [Å] and angles [°] of $[Mn_2(L^2)_2(\mu\text{-}OMe)_2(HOMe)_2]$ (**2**).

Mn(1)-O(1)	1.881(3)
Mn(1)-O(3)	1.896(3)
Mn(1)-O(2)	1.927(2)
Mn(1)-N(1)	1.987(3)
Mn(1)-O(3)#1	2.242(3)
Mn(1)-O(4)	2.244(3)
O(1)-Mn(1)-O(3)	96.45(11)
O(1)-Mn(1)-O(2)	168.88(12)
O(3)-Mn(1)-O(2)	93.49(11)
O(1)-Mn(1)-N(1)	91.06(12)
O(3)-Mn(1)-N(1)	170.26(12)
O(2)-Mn(1)-N(1)	79.64(12)
O(1)-Mn(1)-O(3)#1	97.39(11)
O(3)-Mn(1)-O(3)#1	80.79(10)
O(2)-Mn(1)-O(3)#1	89.10(10)
N(1)-Mn(1)-O(3)#1	92.13(11)
O(1)-Mn(1)-O(4)	85.54(11)
O(3)-Mn(1)-O(4)	97.78(11)
O(2)-Mn(1)-O(4)	88.19(11)
N(1)-Mn(1)-O(4)	88.96(12)
O(3)#1-Mn(1)-O(4)	176.86(9)
N(2)-N(1)-Mn(1)	115.4(2)

Symmetry transformations used to generate equivalent atoms:
#1 -x+1,-y+1,-z+1

Table S3.2. Hydrogen bonding interactions of **2**.

D-H...A	d(D-H)	d(H...A)	d(D...A)	<(DHA)
O(3)-H(3A)...N(1)#1	0.84	2.34	3.050(4)	143.1
O(4)-H(4A)...N(3)#2	0.84	1.91	2.746(4)	176.5

#1 -x+1,-y+1,-z+1 #2 x,y+1,z

Table S4. Selected bond lengths [Å] and angles [°] of $[Mn(L^3)(OMe)]_n$ (**3**).

Mn(1)-O(1)	1.887(4)
Mn(1)-O(3)	1.890(4)
Mn(1)-N(3)	1.974(4)
Mn(1)-O(2)	1.978(4)
Mn(1)-O(3)#1	2.218(4)
Mn(1)-N(1)	2.313(5)
Mn(2)-O(5)	1.887(4)
Mn(2)-O(6)	1.895(4)
Mn(2)-O(4)	1.946(4)
Mn(2)-N(6)	1.984(4)
Mn(2)-O(6)#2	2.229(4)
Mn(2)-N(2)#3	2.383(5)
O(1)-Mn(1)-O(3)	94.16(17)
O(1)-Mn(1)-N(3)	89.99(18)
O(3)-Mn(1)-N(3)	174.93(16)
O(1)-Mn(1)-O(2)	168.30(14)
O(3)-Mn(1)-O(2)	96.74(16)
N(3)-Mn(1)-O(2)	79.35(17)
O(1)-Mn(1)-O(3)#1	100.04(16)
O(3)-Mn(1)-O(3)#1	81.79(16)
N(3)-Mn(1)-O(3)#1	94.63(16)
O(2)-Mn(1)-O(3)#1	85.75(16)
O(1)-Mn(1)-N(1)	91.55(17)
O(3)-Mn(1)-N(1)	90.59(16)
N(3)-Mn(1)-N(1)	92.21(17)
O(2)-Mn(1)-N(1)	84.11(17)
O(3)#1-Mn(1)-N(1)	166.52(13)
O(5)-Mn(2)-O(6)	96.79(17)
O(5)-Mn(2)-O(4)	166.20(15)
O(6)-Mn(2)-O(4)	94.92(16)
O(5)-Mn(2)-N(6)	90.22(18)
O(6)-Mn(2)-N(6)	169.02(15)
O(4)-Mn(2)-N(6)	79.36(16)
O(5)-Mn(2)-O(6)#2	96.01(16)
O(6)-Mn(2)-O(6)#2	80.61(16)
O(4)-Mn(2)-O(6)#2	93.09(15)
N(6)-Mn(2)-O(6)#2	90.28(16)
O(5)-Mn(2)-N(2)#3	86.71(17)
O(6)-Mn(2)-N(2)#3	94.66(16)
O(4)-Mn(2)-N(2)#3	85.07(16)
N(6)-Mn(2)-N(2)#3	94.17(17)
O(6)#2-Mn(2)-N(2)#3	174.78(13)

Symmetry transformations used to generate equivalent atoms:
#1 -x+1,-y+1,-z+2 #2 -x,-y+2,-z+1 #3 -x+1,-y+1,-z+1

Table S5. Selected bond lengths (Å) and bond angles (°) of $[Mn_{10}(L^4)_8(OL^4)_2(DMF)_4(MeOH)_4(H_2O)_2]$ (**4**).

Mn1—O6	1.872 (4)	Mn2—O24	1.839 (4)	Mn3—O21	1.872 (4)
Mn1—O8	1.930 (4)	Mn2—O4	1.904 (4)	Mn3—O7	1.910 (4)
Mn1—N3	1.950 (5)	Mn2—N7	1.950 (5)	Mn3—N5	1.938 (5)
Mn1—O3	1.963 (4)	Mn2—O5	1.954 (4)	Mn3—O2	1.940 (4)
Mn1—O10	2.250 (4)	Mn2—O15	2.251 (5)	Mn3—O9	2.286 (5)
Mn1—N2	2.320 (5)	Mn2—N4	2.367 (5)	Mn3—N8	2.345 (5)
Mn4—O16	1.842 (6)	Mn5—O13	1.846 (5)	Mn5—N1	1.953 (5)
Mn4—O19	1.913 (7)	Mn5—O11	1.933 (5)	Mn5—O14	1.968 (5)
Mn4—N9	1.940 (6)	Mn5—O17	2.231 (6)	Mn5—N10	2.316 (6)
Mn4—O12	1.952 (5)	Mn4—O18	2.241 (7)	Mn4—N6	2.355 (5)

O6—Mn1—O8	170.22 (18)	O6—Mn1—O10	89.63 (19)	N3—Mn1—N2	108.4 (2)
O6—Mn1—N3	91.18 (19)	O8—Mn1—O10	88.88 (18)	O3—Mn1—N2	73.59 (18)
O8—Mn1—N3	79.29 (19)	N3—Mn1—O10	93.85 (19)	O10—Mn1—N2	157.71 (17)
O6—Mn1—O3	90.64 (18)	O3—Mn1—O10	84.14 (17)	O24—Mn2—O4	170.5 (2)
O8—Mn1—O3	98.82 (18)	O6—Mn1—N2	89.63 (19)	O24—Mn2—N7	91.5 (2)
N3—Mn1—O3	177.28 (19)	O8—Mn1—N2	95.39 (19)	O4—Mn2—N7	79.4 (2)
O24—Mn2—O5	97.17 (19)	O5—Mn2—O15	82.77 (19)	O21—Mn3—O7	171.09 (18)
O4—Mn2—O5	92.08 (19)	O24—Mn2—N4	85.25 (19)	O21—Mn3—N5	91.7 (2)
N7—Mn2—O5	170.2 (2)	O4—Mn2—N4	95.78 (19)	O7—Mn3—N5	79.5 (2)
O24—Mn2—O15	89.8 (2)	N7—Mn2—N4	113.39 (19)	O21—Mn3—O2	92.15 (18)
O4—Mn2—O15	93.3 (2)	O5—Mn2—N4	71.97 (17)	O7—Mn3—O2	96.48 (18)
N7—Mn2—O15	92.8 (2)	O15—Mn2—N4	153.39 (19)	N5—Mn3—O2	174.8 (2)
O21—Mn3—O9	90.03 (19)	N5—Mn3—N8	109.6 (2)	O16—Mn4—O12	94.1 (2)

O7—Mn3—O9	88.65 (19)	O2—Mn3—N8	73.76 (17)	O19—Mn4—O12	95.6 (3)
N5—Mn3—O9	92.37 (19)	O9—Mn3—N8	157.95 (17)	N9—Mn4—O12	170.7 (2)
O2—Mn3—O9	84.20 (17)	O16—Mn4—O19	170.3 (2)	O16—Mn4—O18	94.2 (4)
O21—Mn3—N8	90.95 (19)	O16—Mn4—N9	91.0 (2)	O19—Mn4—O18	86.8 (5)
O7—Mn3—N8	93.58 (18)	O19—Mn4—N9	79.3 (3)	N9—Mn4—O18	90.3 (3)
O12—Mn4—O18	81.6 (2)	O13—Mn5—O11	170.9 (2)	O13—Mn5—O17	88.2 (2)
O16—Mn4—N6	91.7 (2)	O13—Mn5—N1	91.4 (2)	O11—Mn5—O17	92.3 (2)
O19—Mn4—N6	91.5 (3)	O11—Mn5—N1	79.4 (2)	N1—Mn5—O17	90.7 (2)
N9—Mn4—N6	114.6 (2)	O13—Mn5—O14	93.7 (2)	O14—Mn5—O17	85.3 (2)
O12—Mn4—N6	73.0 (2)	O11—Mn5—O14	95.4 (2)	O13—Mn5—N10	91.6 (2)
O18—Mn4—N6	154.3 (3)	N1—Mn5—O14	173.3 (2)	O11—Mn5—N10	91.2 (2)
N1—Mn5—N10	110.3 (2)	O14—Mn5—N10	73.9 (2)	O17—Mn5—N10	159.1 (2)

2. BVS calculations

Bond valence sum (BVS) values was calculated for each Mn centers in **1**, **2**, **3** and **4** respectively. The calculations were performed with the help of standard relevant parameters reported in the literature.[1,2]

Table S6.1. BVS calculations of **1.**

A_i- B_j	R(Å)	S_{ij}	ΣS_{ij}	Conclusion
Mn(1)-O(1)	1.928	0.635	3.304	Mn(III)
Mn(1)-O(3)	2.178	0.323		
Mn(1)-O(2)	1.925	0.640		
Mn(1)-O(4)	2.172	0.328		
Mn(1)-O(6)	1.893	0.698		
Mn(1)-N(1)	1.972	0.684		
A_i- B_j	R(Å)	S_{ij}	ΣS_{ij}	Conclusion
Mn(2)-O(6)	1.897	0.691		

Mn(2)-O(8)	2.234	0.277	3.101	Mn(III)
Mn(2)-O(6)	1.891	0.701		
Mn(2)-O(10)	2.257	0.261		
Mn(2)-O(9)	1.957	0.587		
Mn(2)-N(7)	1.959	0.584		

Table S6.2. BVS Calculations for **2.**

A_i- B_j	R(Å)	S_{ij}	ΣS_{ij}	Conclusion
Mn(1)-O(2)	1.927	0.637	3.250	Mn(III)
Mn(1)-O(3)	1.896	0.692		
Mn(1)-O(3)	2.242	0.272		
Mn(1)-O(1)	1.881	0.721		
Mn(1)-N(1)	1.987	0.658		
Mn(1)-O(4)	2.244	0.270		

Table S6.3. BVS Calculations for **3.**

A_i- B_j	R(Å)	S_{ij}	ΣS_{ij}	Conclusion
Mn(1)-O(3)	2.218	0.290	3.212	Mn(III)
Mn(1)-O(3)	1.890	0.704		
Mn(1)-O(2)	1.978	0.555		
Mn(1)-O(1)	1.887	0.709		
Mn(1)-N(3)	1.974	0.681		
Mn(1)-N(1)	2.313	0.273		

Table S6.4. BVS Calculations for **4.**

A_i- B_j	R(Å)	S_{ij}	ΣS_{ij}	Conclusion
Mn(1)-N(2)	2.318	0.268	3.207	Mn(III)
Mn(1)-N(3)	1.954	0.719		
Mn(1)-O(3)	1.961	0.580		
Mn(1)-O(6)	1.871	0.740		
Mn(1)-O(8)	1.928	0.635		
Mn(1)-O(10)	2.251	0.265		
A_i- B_j	R(Å)	S_{ij}	ΣS_{ij}	Conclusion
Mn(3)-N(5)	1.936	0.754	3.252	Mn(III)
Mn(3)-N(8)	2.340	0.253		
Mn(3)-O(2)	1.945	0.606		
Mn(3)-O(7)	1.911	0.664		
Mn(3)-O(9)	2.279	0.245		
Mn(3)-O(21)	1.876	0.730		

A_i- B_j	R(Å)	S_{ij}	ΣS_{ij}	Conclusion
Mn(2)-N(4)	2.375	0.230	3.288	Mn(III)
Mn(2)-N(7)	1.952	0.723		
Mn(2)-O(5)	1.960	0.582		
Mn(2)-O(4)	1.902	0.681		
Mn(2)-O(24)	1.838	0.809		
Mn(2)-O(15)	2.253	0.263		
A_i- B_j	R(Å)	S_{ij}	ΣS_{ij}	Conclusion

Mn(5)-N(1)	1.956	0.715	3.265	Mn(III)	
Mn(5)-N(10)	2.312	0.273			
Mn(5)-O(11)	1.926	0.638			
Mn(5)-O(13)	1.847	0.790			
Mn(5)-O(14)	1.967	0.571			
Mn(5)-O(17)	2.233	0.278			

A_i- B_j	R(Å)	S_{ij}	ΣS_{ij}	Conclusion
Mn(4)-N(6)	2.350	0.246	3.303	Mn(III)
Mn(4)-N(9)	1.944	0.738		
Mn(4)-O(18)	2.247	0.268		
Mn(4)-O(12)	1.950	0.598		
Mn(4)-O(16)	1.847	0.790		
Mn(4)-O(19)	1.912	0.663		

3. Powder X-ray Diffraction studies

The crystals of complexes **1**-**4** were grounded gently using mortar and pestle to make them into a powdered form. About 30 mg of powdered sample of complexes **1**-**4** were taken on a quartz plate and their powder X-ray diffraction pattern were recorded using Bruker D8 advance PXRD in the 2θ range of 5° to 55° under ambient conditions. Each samples were undergone 2 h scanning period to obtain a resolved peak in a peak profile. The powder X-ray diffraction pattern of all the four complexes were discussed below. Among them, the peak profile of the complexes **2** and **3** were compared together to understand their phase and bulk purity. The well

matching spectra of their simulated and experimental pattern suggest that the complexes are pure in bulk phase.

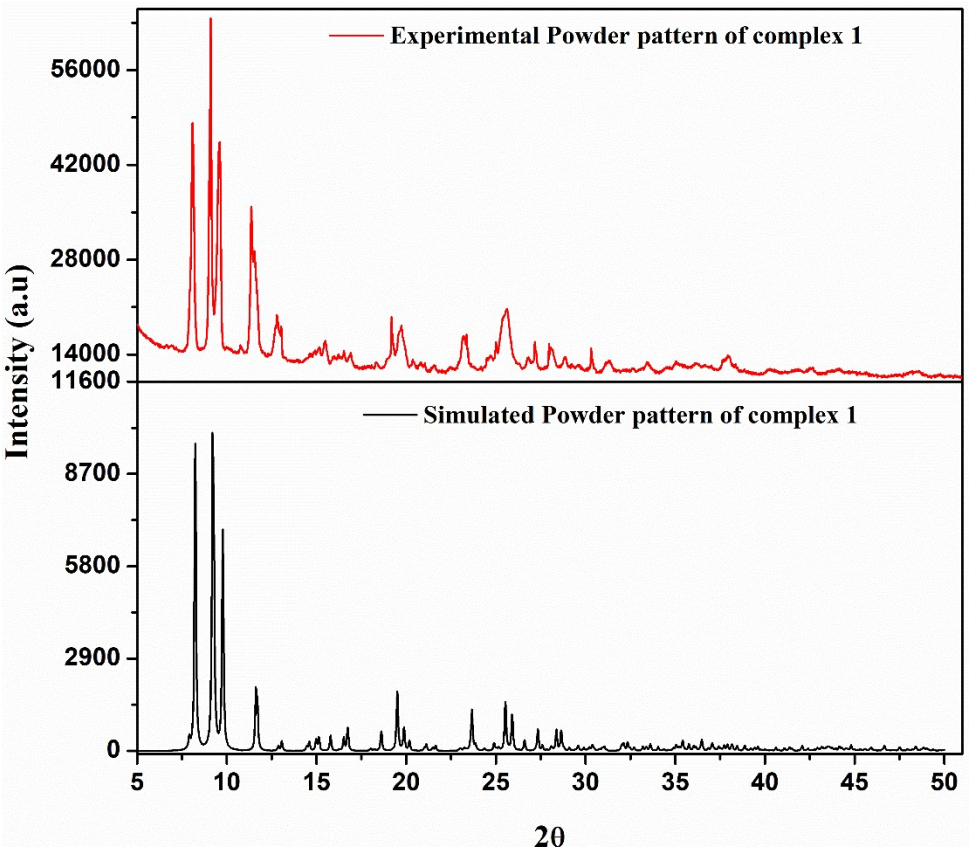

Figure S2. Simulated and experimentally obtained powder X-ray diffraction patterns of complex **1**.

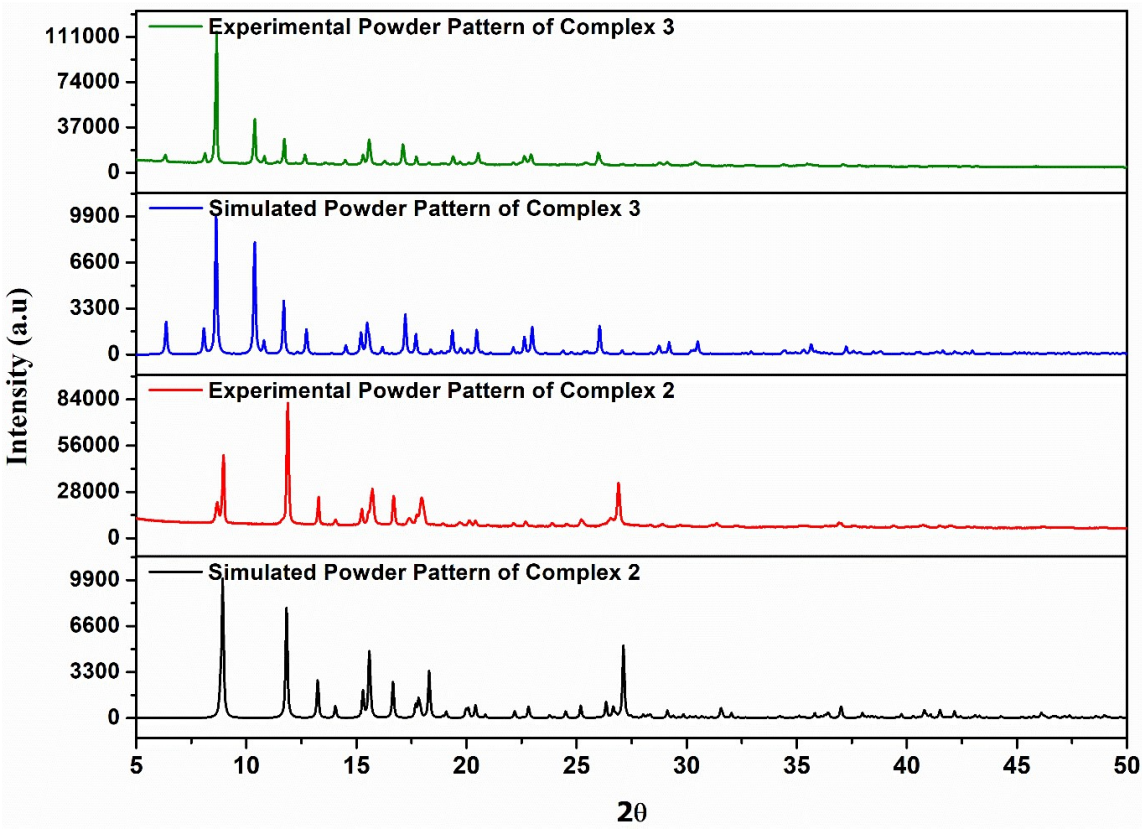

Figure S3. Comparison of simulated and experimentally obtained powder X-ray diffraction patterns of complexes **2** and **3**.

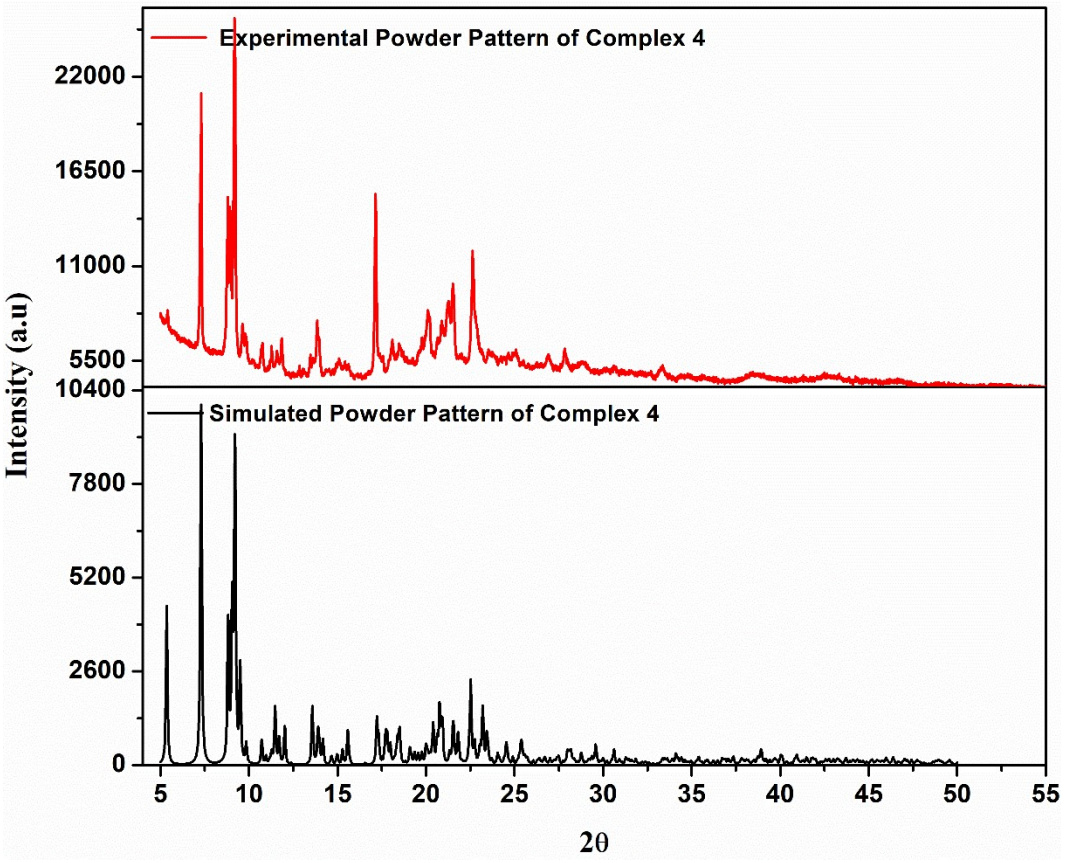

Figure S4. Simulated and experimentally obtained powder X-ray diffraction patterns of complex **4**. The diffraction at 2θ of 17° in the experimental curve is due to the lattice DMF/H_2O molecules which were omitted during structure refinement since they were highly disordered.

4. Infrared spectra

Infrared (IR) spectra was recorded for all the three complexes **1**, **2** and **3** in the region of 500-3500 cm^{-1}. It was recorded using Jasco FT-IR-4100 spectrometer by preparing KBr pellet. The samples were grounded well in order to make it a fine powder and kept under the sodium lamp for few minutes. Then by using pressurized pellet making machine disk like pellets were made and carried out the analysis. The strong and broad absorptions observed for **1**, **2** and **3** in the range 3400-3500 cm^{-1} indicate the presence of free –OH or H_2O. Sharp peaks obtained 1500-1600 cm^{-1} shows C=C stretching. Absorptions of 2943 and 3082 cm^{-1} in the non-coordinated ligands are missing in **1, 2** and **3,** indicating the coordination of Ar-O^- to the metal centre. The shifting of free $\upsilon_{C=N}$ to lower region in all the three complexes is due to the presence of coordinated imine with metal. Likewise, the υ_{C-O} appears in the region 1240-1290 cm^{-1} in the free ligand shifted to a lower frequency region in the complexes, indicate the participation of phenolic oxygen in C-O-M formation. The new vibrations obtained in the region 400-600 cm^{-1} in **1**, **2** and **3** are assigned as M-O and M-N frequencies.

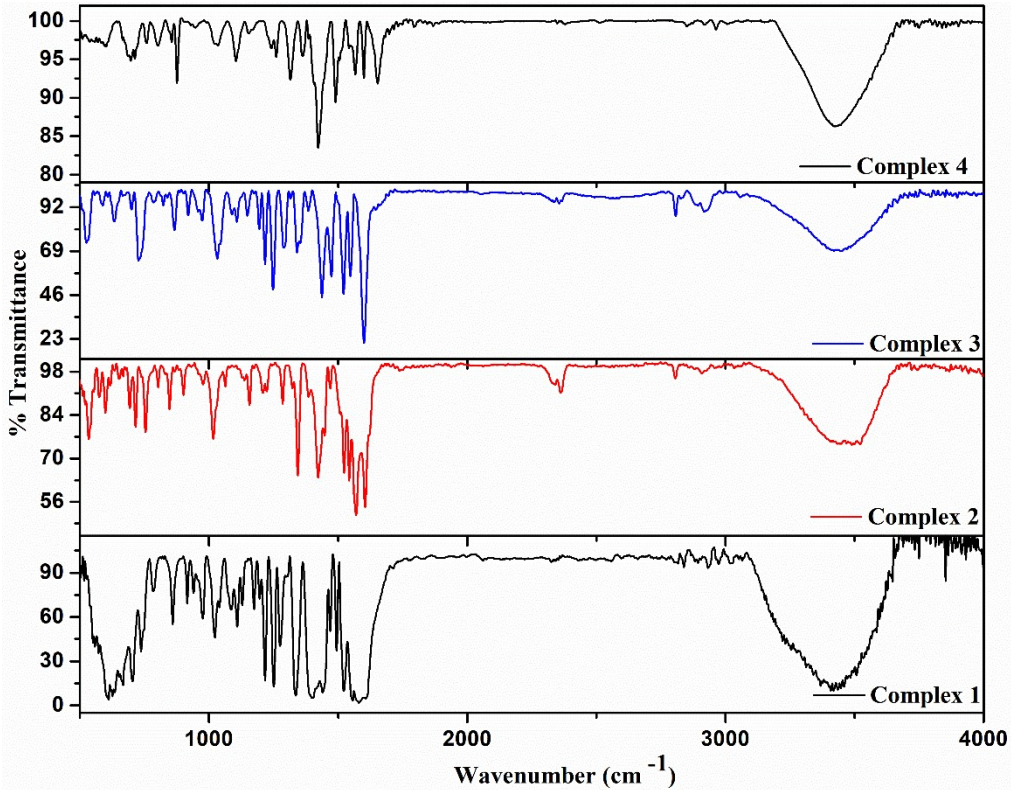

Figure S5. FT-IR spectra of **1**, **2** and **3** and **4.**

Table S7. IR stretching frequencies of **1**, **2**, **3** and **4** are given below.

Complexes	$\upsilon_{Ar\text{-}OH/H2O}$	$\upsilon_{C=C}$	$\upsilon_{C=N}$	$\upsilon_{C\text{-}O}$	$\upsilon_{C\text{-}H}$ Out of plane bending
Complex **1**	3417 cm^{-1}	1581 cm^{-1}	1595 cm^{-1}	1024 cm^{-1}	849 cm^{-1}
Complex **2**	3478 cm^{-1}	1573 cm^{-1}	1608 cm^{-1}	1017 cm^{-1}	759 cm^{-1}
Complex **3**	3542 cm^{-1}	1602 cm^{-1}	1612 cm^{-1}	1248 cm^{-1}	729 cm^{-1}
Complex **4**	3423 cm^{-1}	1567 cm^{-1}	1601 cm^{-1}	1033 1	758 cm^{-1}

5. UV-Visible measurements

The UV-Visible spectra of **1**, **2**, **3** and **4** was recorded by dissolving those in MeOH solvent to study the possible transitions in the visible region. The absorption bands obtained in each of their spectra is by dissolving the samples with methanol in a 3.5 mL cuvette with a path length of 1cm at ambient temperature and which were recorded by using Jasco V-650 UV-Visible

spectrometer. From the range of 350-900 nm the corresponding spectra were recorded.

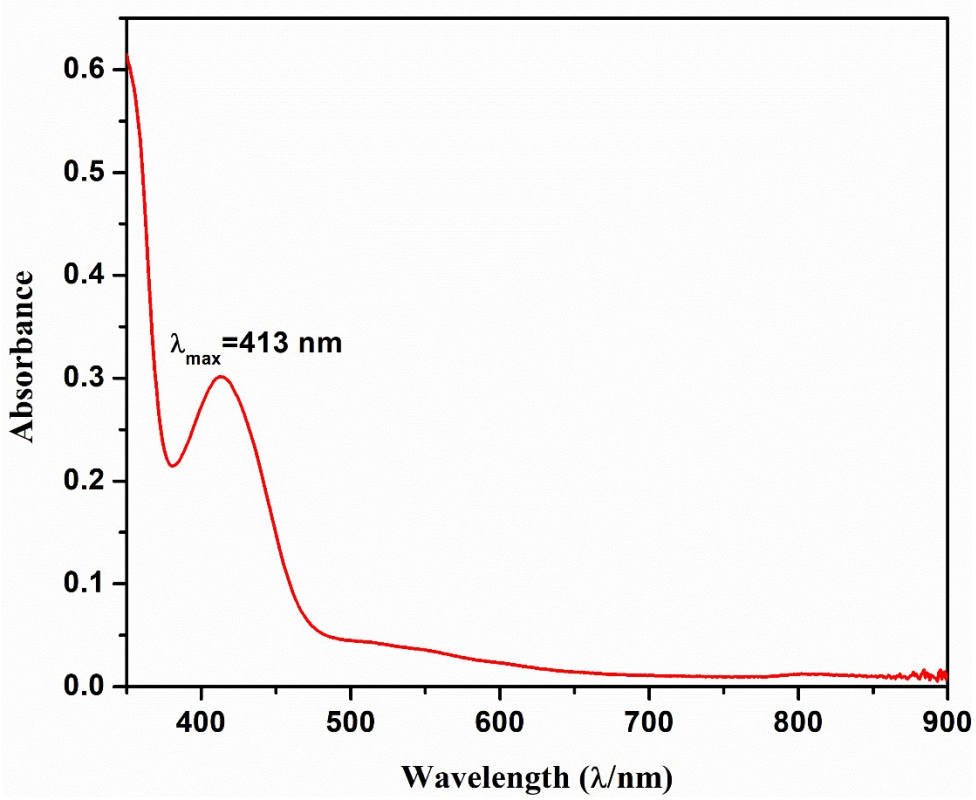

Figure S6. UV-Vis spectrum of **1** in MeOH.

The peak corresponds to the cut-off wavelength of the solvent was not considered and hence it is not shown. The λ_{max} absorption at around 413 nm is due to the azo (N=N-) group which might be conjugated with the aromatic π system.

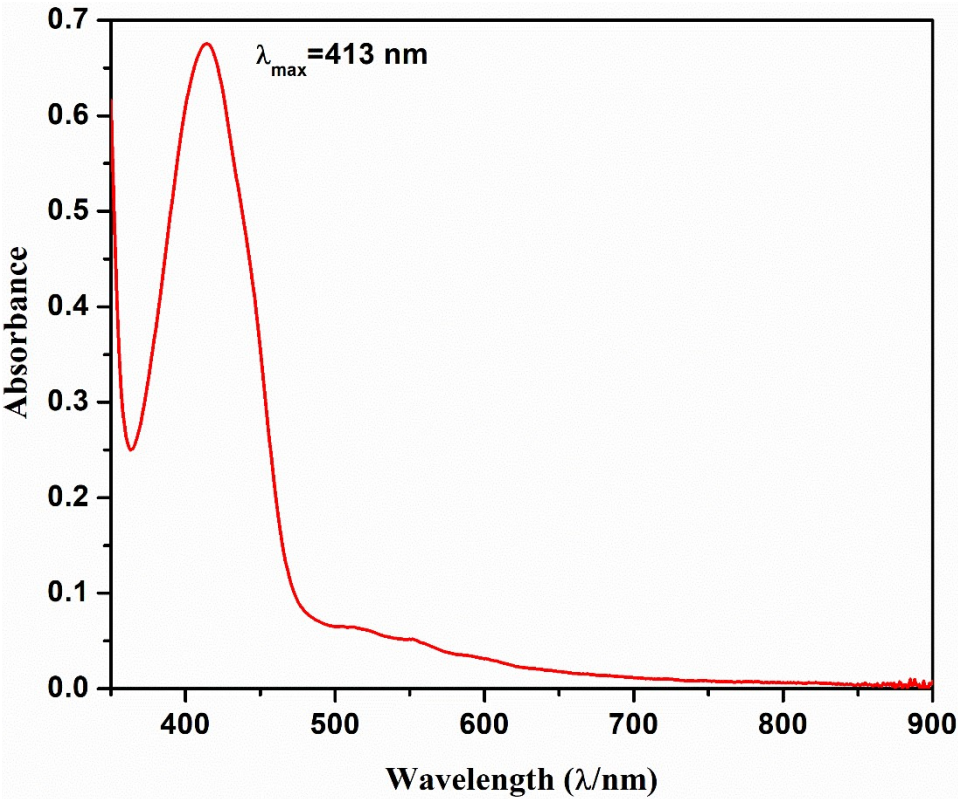

Figure S7. UV-Vis spectrum of **2** in MeOH.

The UV-Visible spectrum of **2** shows absorptions at about 413 nm corresponding to the azo group participation in conjugation with the aromatic system.

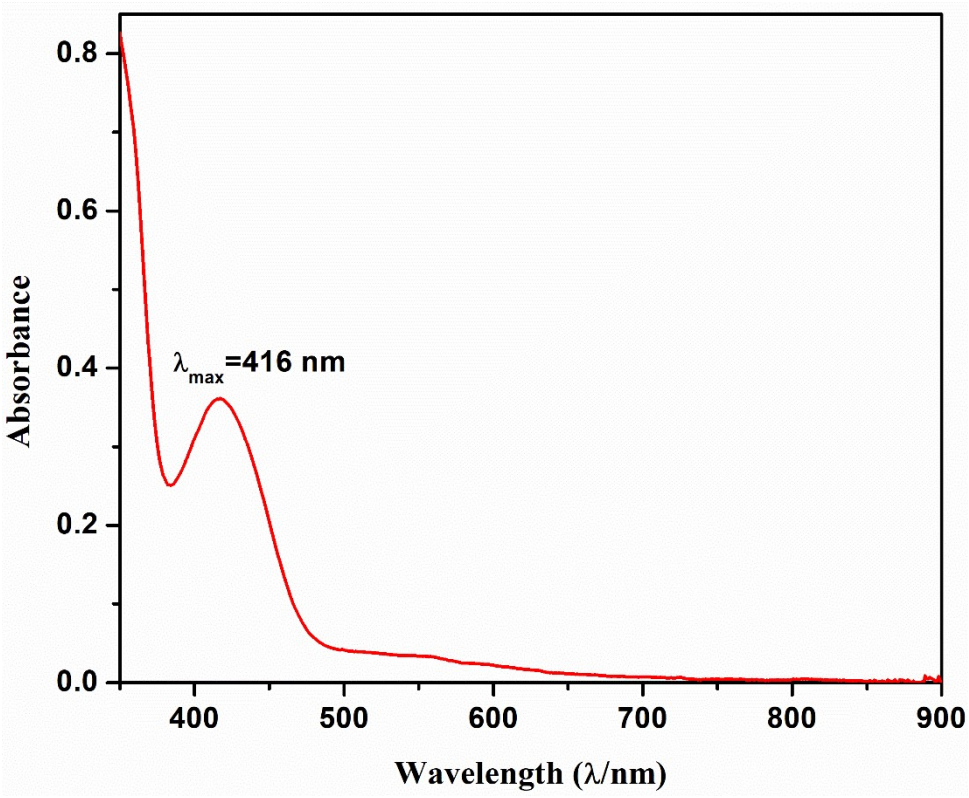

Figure S8. UV-Vis spectrum of **3** in MeOH.

The UV-Visible spectrum of **3** shows λ_{max} absorption at 415 nm due to the possible conjugation of -N=N- with the π aromatic ring system.

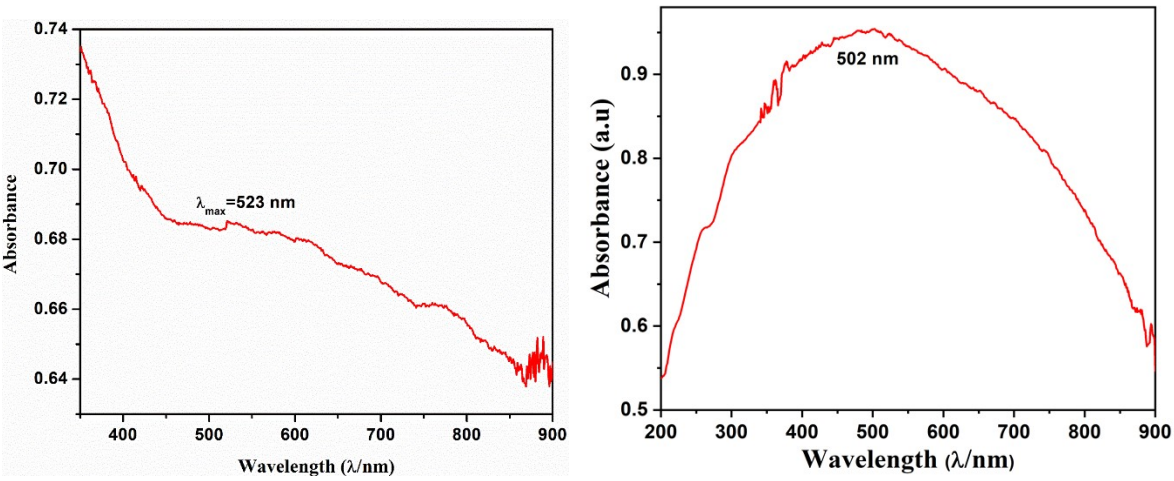

Figure S9. UV-Vis spectrum of diluted solution (left) of **4** in MeOH. DRS solid state UV-Vis spectrum of **4** (right).

The UV-Visible spectrum of **4** shows a weak band at 523 nm due to the probable n →π* transition of -C=S- group with in the conjugated π aromatic ring system of ligand molecule.

6. Thermo-gravimetric analysis of complexes

Thermo-gravimetric analysis of the complexes **1-3** was recorded by heating 4.5-5 mg of each sample from the room temperature to 900 °C at a heating rate of 20 °C under the flow of nitrogen at the flow rate of 60 mL/min on TA Instruments model-Q500. The TGA of complex **4** was carried out under areal atmosphere.

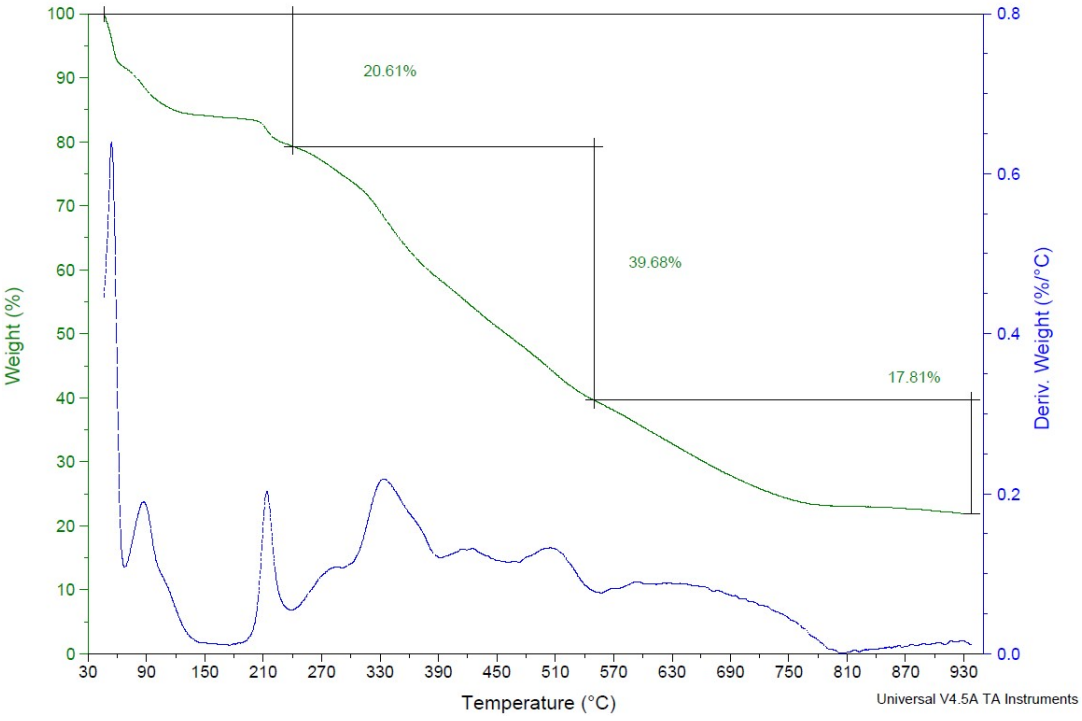

Figure S10. TGA plot of complex **1.**

In the TGA plot of complex **1**, the first step of weight loss was 20.61% at 220 °C due to the loss of one ligand (calculated weight %: 20.35). When there is a further increase in temperature from 220-510 °C, a considerable weight loss observed around 39.68% suggests the loss of two Mn atoms along with a ligand and four coordinated solvent methanol molecules (calculated weight %: 38.11). 17.81% of weight loss at the final step matches with the elimination of four bridged acetate molecules (calculated weight %: 17.91).

TGA plot of complex **2**, shows sequential weight losses such as 17.54 %, 39.37 %, and 13.31 % in the first, second and third steps respectively. The first weight loss of 17.54 % was observed in the range of 270-340 °C due to the loss of coordinated solvent methanol molecules and phenyl part of one of the ligands coordinated to metal (calculated weight %: 17.92). Second weight loss (39.37 %) was noticed from 390-500 °C due to the removal of the remaining part of the first ligand, methyl moiety, and another ligand leaving behind oxide with the metal (calculated weight %: 39.95).

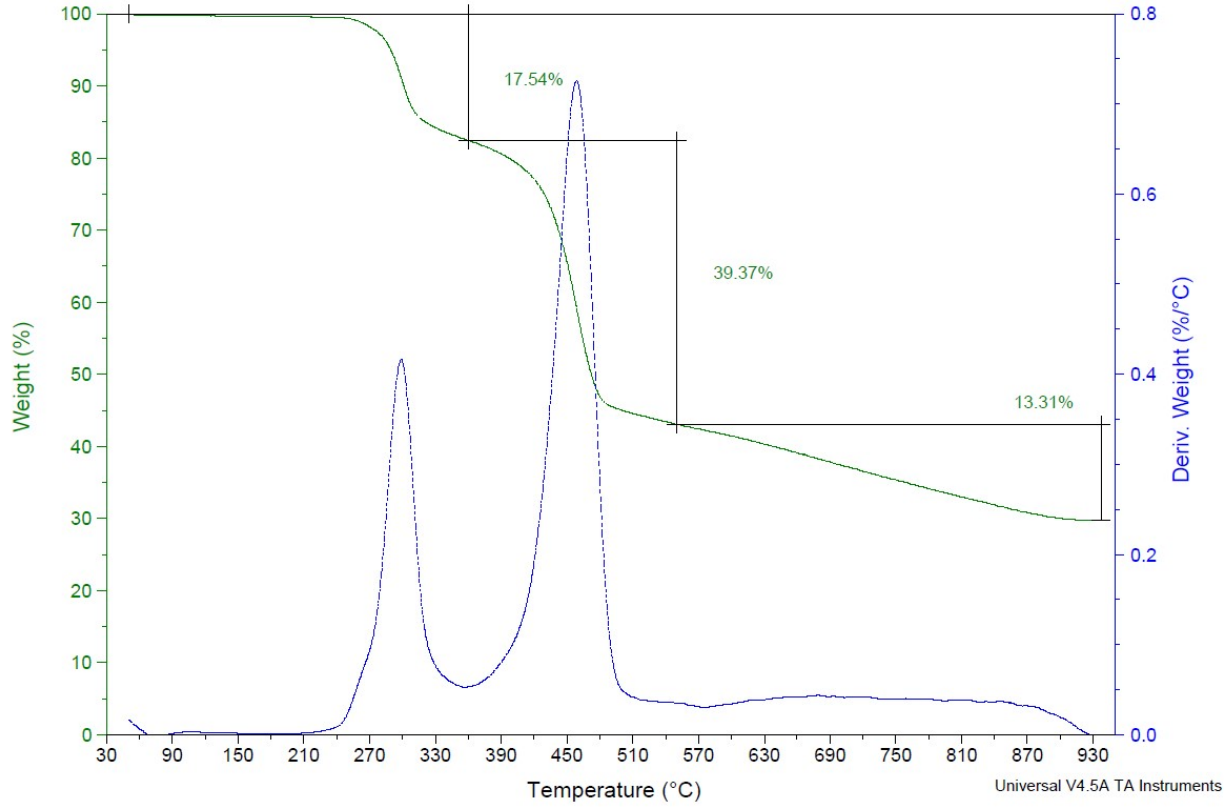

Figure S11. TGA plot of complex **2**.

Further temperature ramping above 550 °C, resulting the weight loss of 13.31 % due to the loss of methyl group of bridged methoxy and two metals. (Calculated weight %: 14.06)

In TGA plot of complex **3,** the first loss of 9.515 % was due to the weight loss of two methoxy

groups, which was observed in the range of 220-300 °C (Calculated weight %: 8.72). When the temperature ramped to 400 °C, we noticed a 22.75 % weight loss due to the detachment of part of the organic moiety from one of the ligands (Calculated weight %: 22.80). Then finally, 28.50 % of the loss was due to the decomposition of part of another ligand leaving behind pyridine moiety and two methoxy groups (Calculated weight %: 29.4).

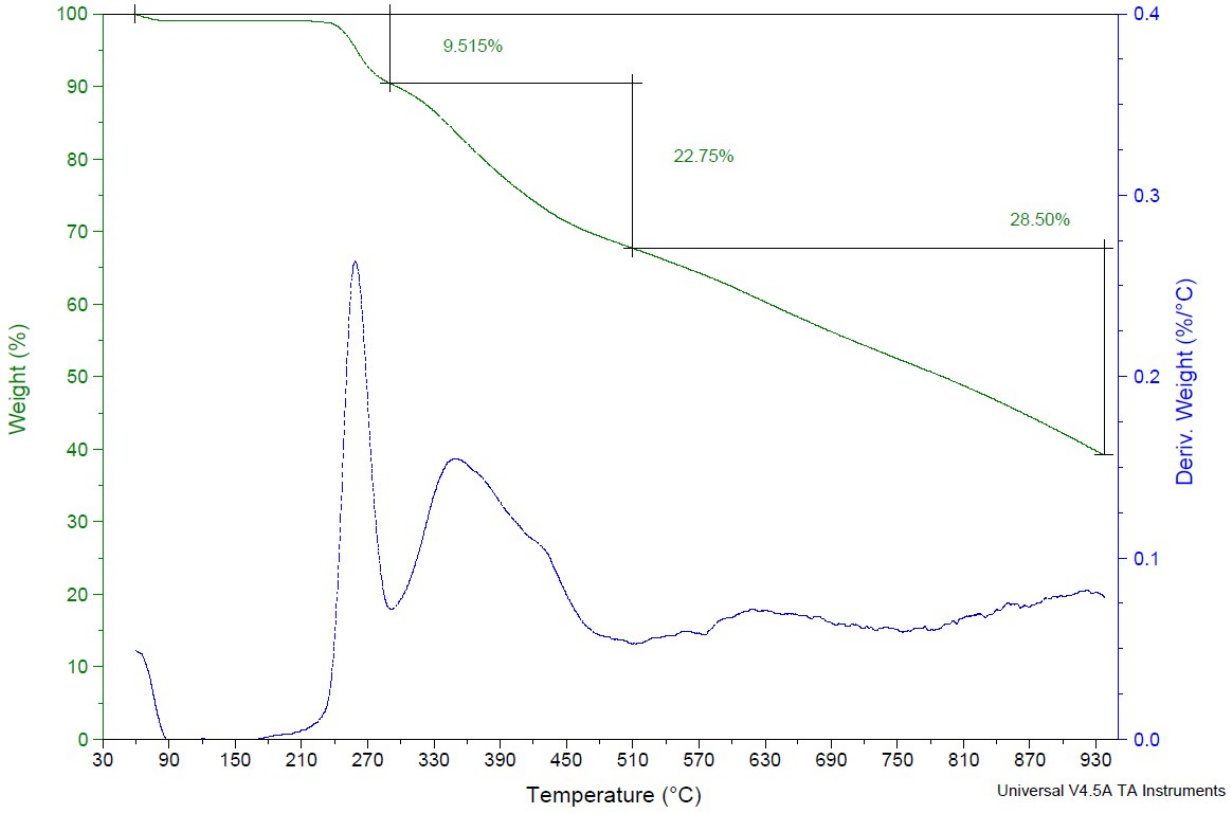

Figure S12. TGA Plot of Complex **3**

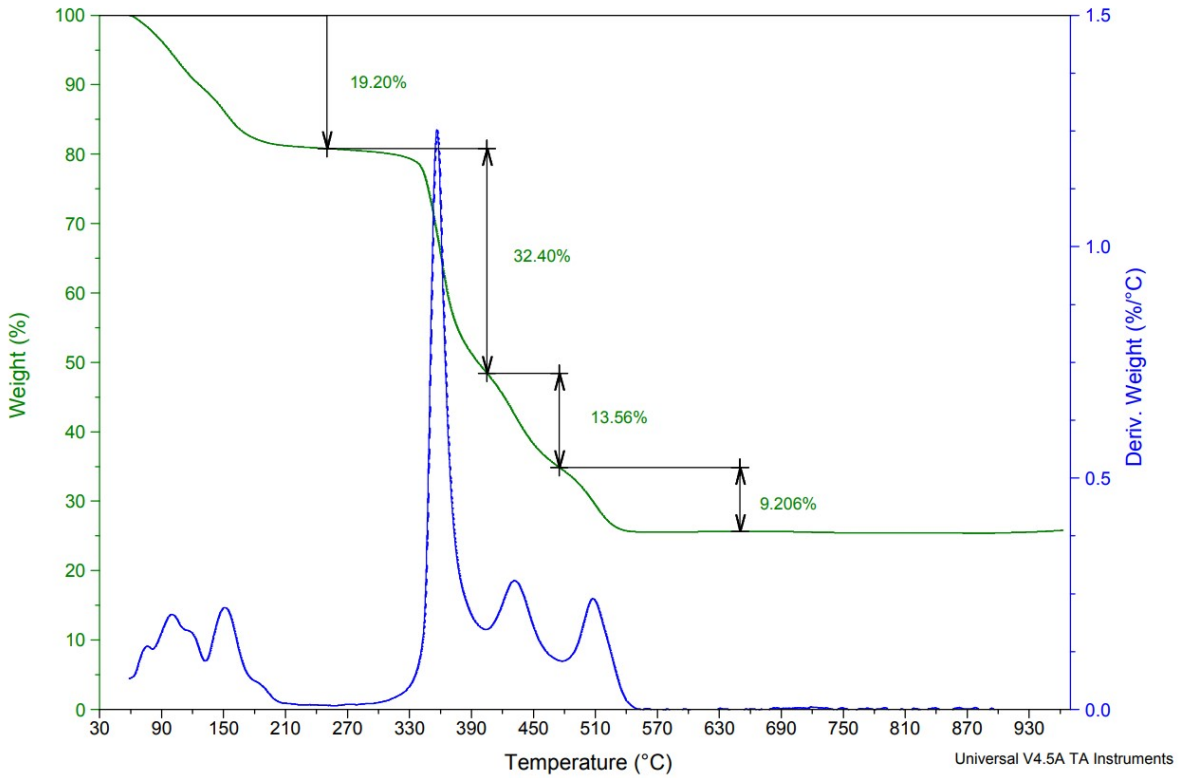

Figure S13. TGA Plot of complex $[Mn_{10}(L^4)_8(OL^4)_2(DMF)_4(MeOH)_4(H_2O)_2]$ (**4**) under air. TGA was performed under areal condition. The first step in the thermal loss of a complex $[Mn_{10}(L^4)_8(OL^4)_2(DMF)_4(MeOH)_4(H_2O)_2]$ (**4**) undergoes loss of coordinated solvents and lattice solvents in the temperature range of 40-200 °C. This weight loss of 19.20 % closely matches with the loss of four coordinated DMF, four MeOH, two H_2O molecules and additional lattice solvents (2 DMF and one H_2O molecules which were omitted during structure refinements since they are disordered) leading to the formation of $[Mn_{10}(L^4)_8(OL^4)_2]$. It is stable in the temperature of 200-300 °C and subsequently it undergoes loss of organic ligands 550 °C leading to the formation of α-Mn_2O_3 as the most stable product (see section 10 for powder XRD pattern).

7. Magnetic Plots of complexes 1-3:

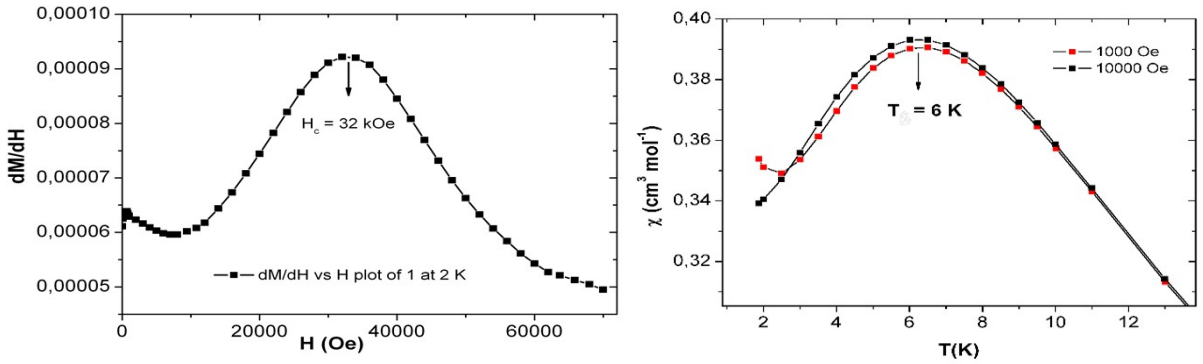

Figure S14. Plots of *dM/dH* vs *H* (left) and χ vs *T* (right) of complex **1**.

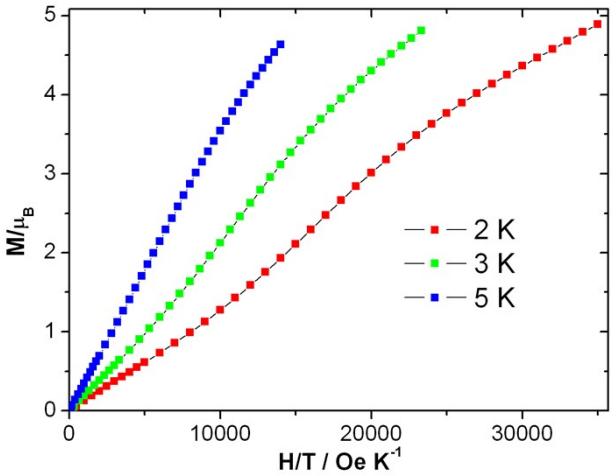

Figure S15. Plots of *M* vs *H/T* at indicated temperature of complex **1**.

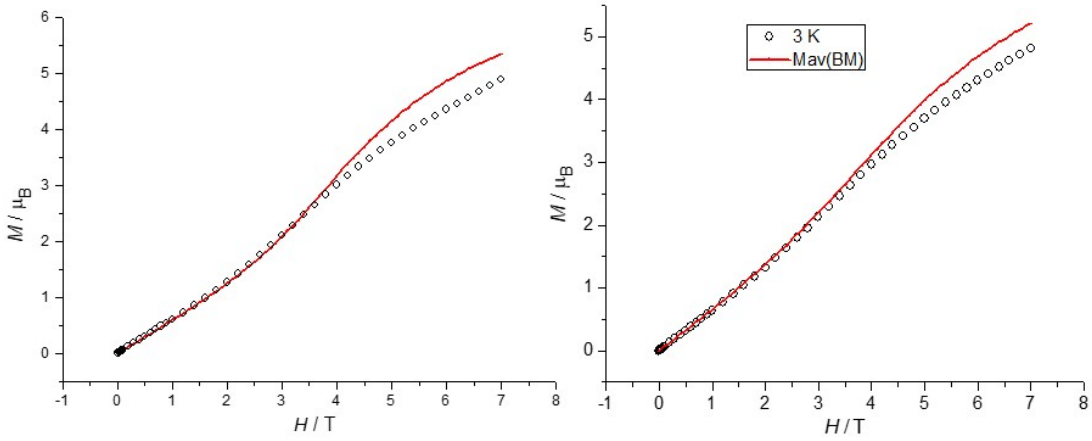

Figure S16. Fit of *M* vs *H* plots of **1** at 2 K (left) and 3 K (right). Proposed field dependent spin structures of complex **1** (bottom). The arrows represent the Jahn-Teller anisotropic magnetic axis.

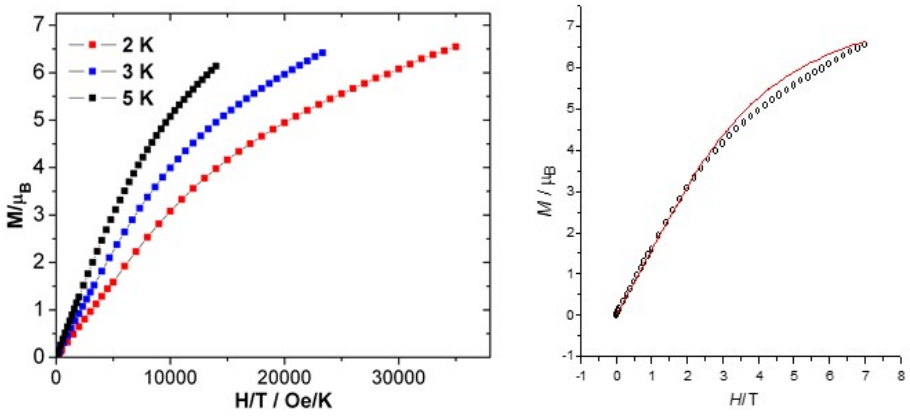

Figure S17. Plots of *M* vs *H/T* (left) and fit of *M* vs *H* plot of **2** at 2 K (right).

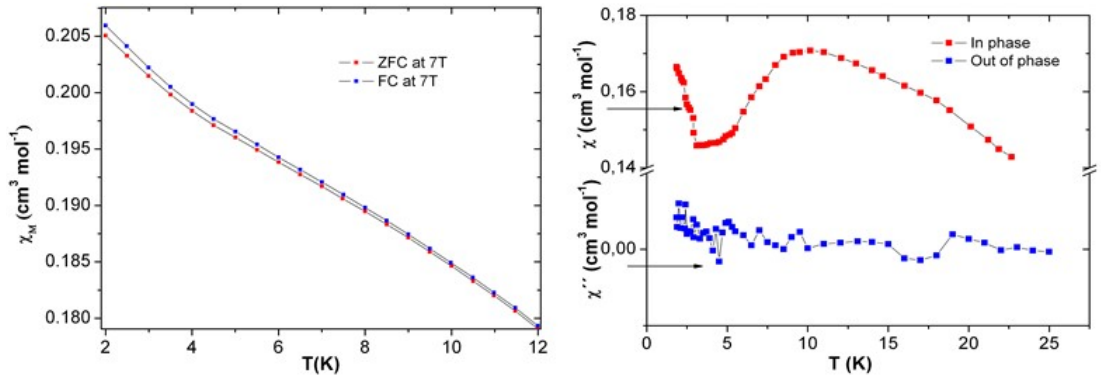

Figure S18. Plots of ZFC and FC susceptibilities vs T of **2** at 70 kOe (left). Plots χ', χ'' vs *T* of **2** under dc field = 3 Oe (right). Frequency of 1000 Hz.

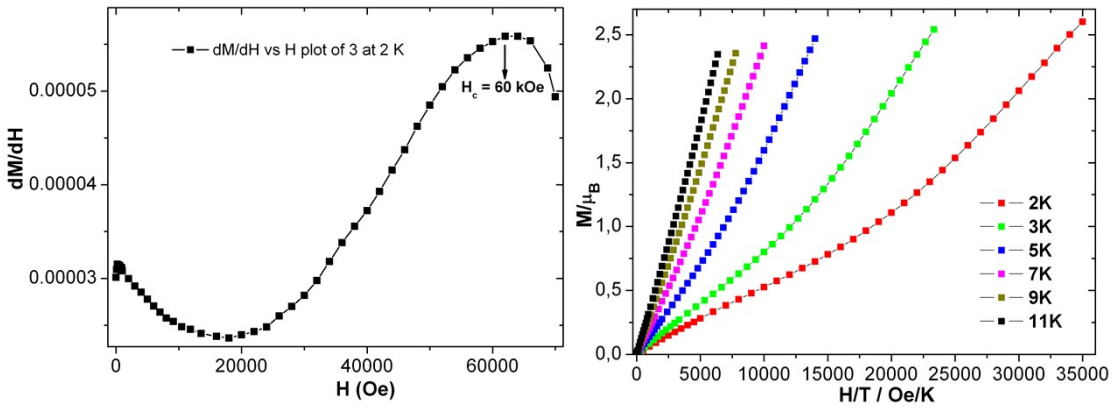

Figure S19. Plots of *dM/dH* vs *H* of **3** at 2 K (left) and *M* vs *H/T* (right)

.....

8. Theoretical calculations:

Table S8. BS-DFT computed energies of high-spin and six broken-symmetry solution on the X-ray crystal structure of complex **1**. Here we have chosen six broken-symmetry solutions to extract the *J* value using the H = $-2JS_1S_2$ formalism.

Solutions	Energy (cm^{-1})	ρ^{Mn1}	ρ^{Mn2}	ρ^{Mn3}	ρ^{Mn4}	$\langle S^2 \rangle$
HS	-7991.51590	3.77	3.81	3.77	3.81	72.1365
BS1	-7991.51734	**-3.73**	3.79	3.77	3.79	24.0988
BS2	-7991.51983	3.75	**-3.76**	3.75	3.80	24.0795
BS3	-7991.51734	3.77	3.79	**-3.73**	3.79	24.0988
BS4	-7991.51983	3.75	3.80	3.75	**-3.76**	24.0795
BS5	-7991.51989	**-3.75**	**-3.78**	3.75	3.78	8.0783
BS6	-7991.51867	3.73	**-3.77**	3.73	**-3.77**	8.0633

ρ^{Mn} is the spin density on the Mn atom

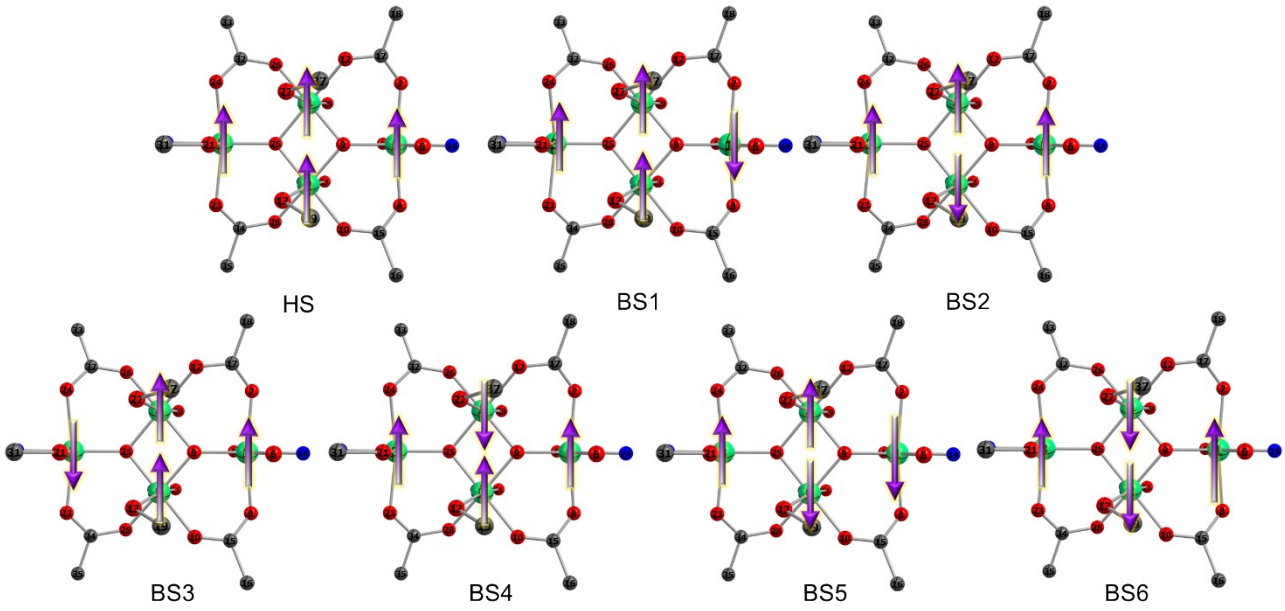

Figure S20. DFT computed different spin configurations of complex **1**. The core structure of the Mn_4 butterfly is shown for clarity. (Color code: Mn -Green; O -red; N-blue; C-grey).

Table S9. DFT computed *J* values along with the corresponding avg. ∠Mn-O-Mn bond angle and ∠Mn-O-Mn-O dihedral angle of complex **1**.

	***J* values (cm^{-1})**	**Average Mn-O-Mn angle (°)**	**Dihedral angle (°)**
J_{wb1}	-7.6	127.6	154.2
J_{wb2}	-7.6	127.4	147.1
J_{bb}	-28.0	99.1	0.0
J_{ww}	-0.6	-	-

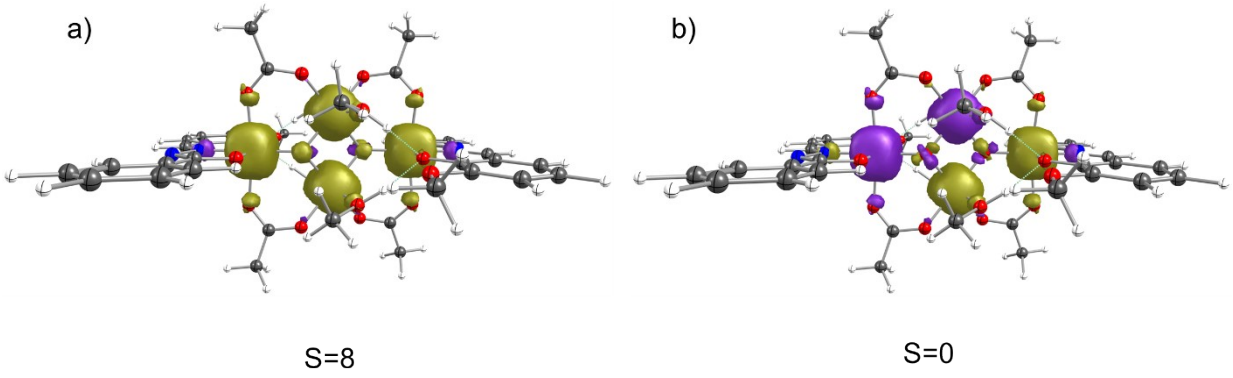

Figure S21. DFT computed spin-density plot of; (a) High Spin (S = 8); (b) Broken Symmetry (S = 0) of complex **1**. The olive green and purple color represent the positive and negative spin density respectively, with an isosurface value of 0.01 e^{-}/$bohr^3$.

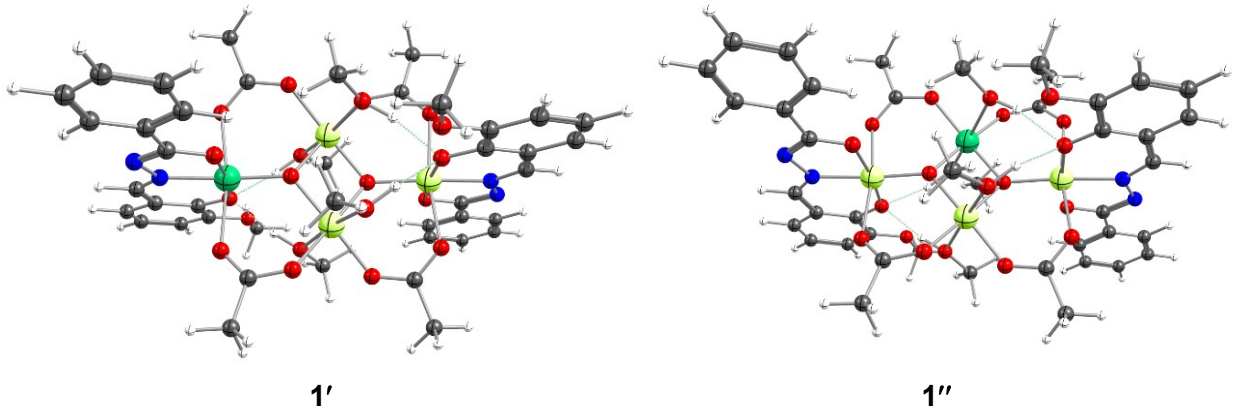

Figure S22. Monomeric models (**1'** and **1''**) prepared from the crystal structure of complexes **1**. The position of hydrogens was optimized using DFT calculations. (Color code: Mn -Green; Ga-yellow; O -red; N-blue; C-grey; H-white)

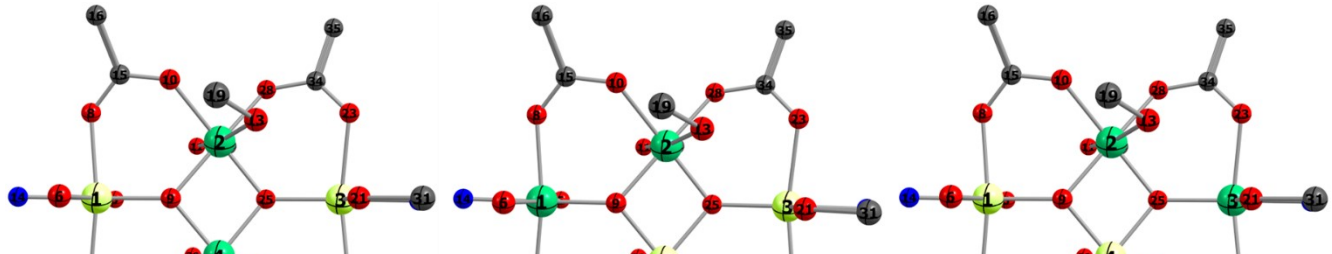

Figure S23. Dimeric models ($\mathbf{1_a}$, $\mathbf{1_b}$, $\mathbf{1_c}$) prepared from the crystal structure of complexes **1**. (Color code: Mn -Green; Ga-yellow; O -red; N-blue; C-grey).

Table S10. BS-DFT computed energies of high-spin and broken-symmetry solution, spin densities, and *J* values for dimeric model $\mathbf{1_a}$ equivalent to J_{bb} interaction of complex **1**.

Solutions	Energy	ρ1	ρ2	ρ3	ρ4	⟨ S²⟩	*J* (cm⁻¹)
HS	-9561.951994	0.01	3.79	0.01	3.79	20.0631	–62.7
BS	-9561.954852	0.00	**-3.78**	0.00	3.78	4.0394	

J values are estimated using the following equation,

$$\boldsymbol{J} = -\frac{E_{HS} - E_{BS}}{2S1\,S2 + S2}$$

Table S11. BS-DFT computed energies of high-spin and broken-symmetry solution, spin densities, and *J* values for model $\mathbf{1_b}$ equivalent to J_{wb1} interaction of complex **1**.

Solutions	Energy	ρ1	ρ2	ρ3	ρ4	⟨ S²⟩	*J* (cm⁻¹)
HS	-9561.944614	3.76	3.81	0.00	0.02	20.0717	–11.03
BS	-9561.945117	3.74	**-3.79**	0.00	0.00	4.0532	

J values are estimated using the following equation,

$$\boldsymbol{J} = -\frac{E_{HS} - E_{BS}}{2S1\,S2 + S2}$$

Table S12. BS-DFT computed energies of high-spin and broken-symmetry solution, spin densities, and *J* values for model $\mathbf{1_c}$ equivalent to J_{wb2} interaction of complex **1**.

Solutions	Energy	ρ1	ρ2	ρ3	ρ4	⟨ S²⟩	*J* (cm⁻¹)
HS	-9561.944654	0.00	3.81	3.76	0.02	20.0718	–11.5
BS	-9561.945176	0.00	**-3.79**	3.74	0.00	4.0527	

J values are estimated using the following equation,

$$J = - \frac{E_{HS} - E_{BS}}{2S1\,S2 + S2}$$

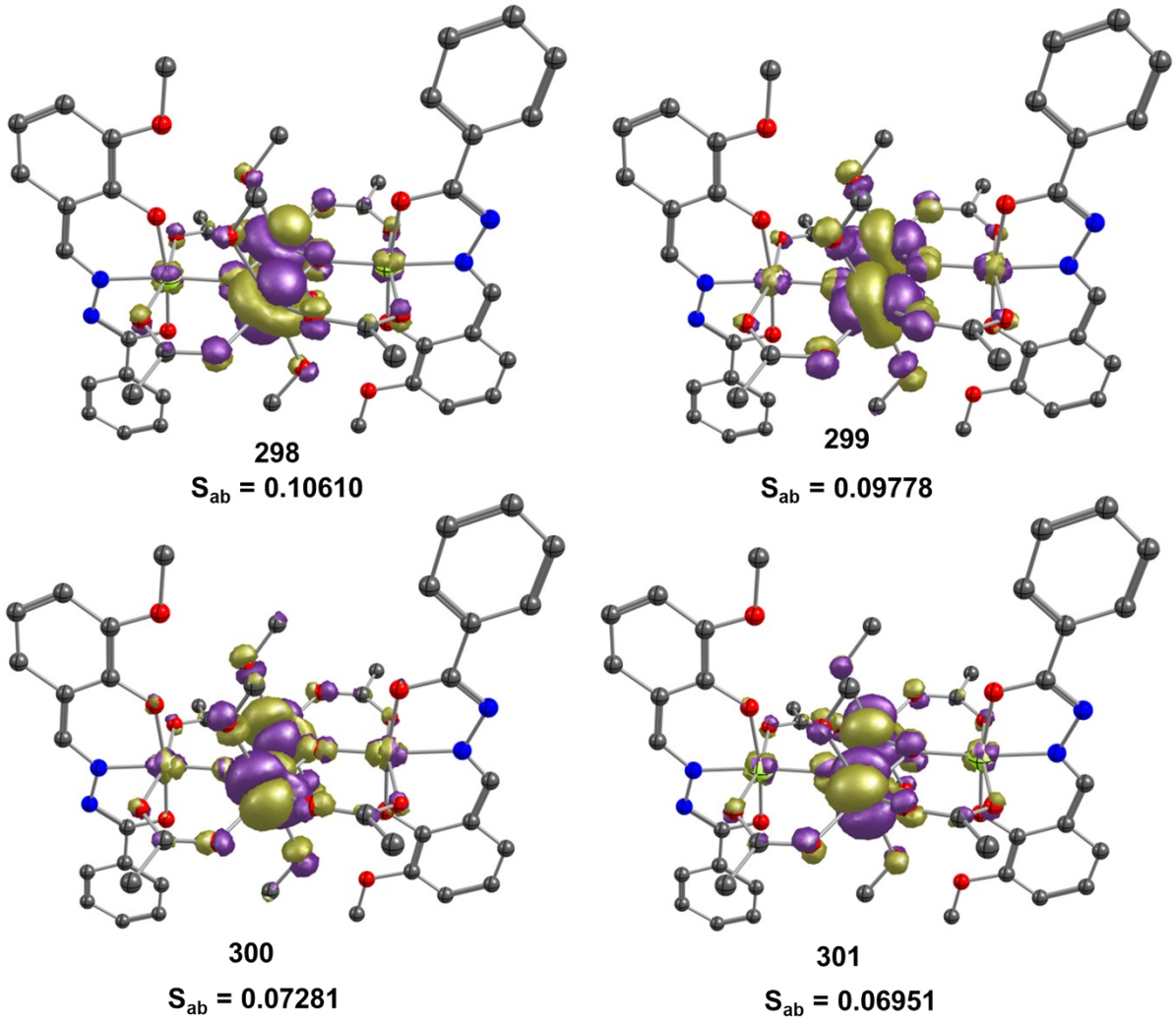

Figure S24. DFT computed corresponding orbitals for which the overlap integral values were calculated for $\mathbf{1_a}$ equivalent to J_{wb2} interaction of complex **1** at contour value = 0.07 e - /bohr^3.

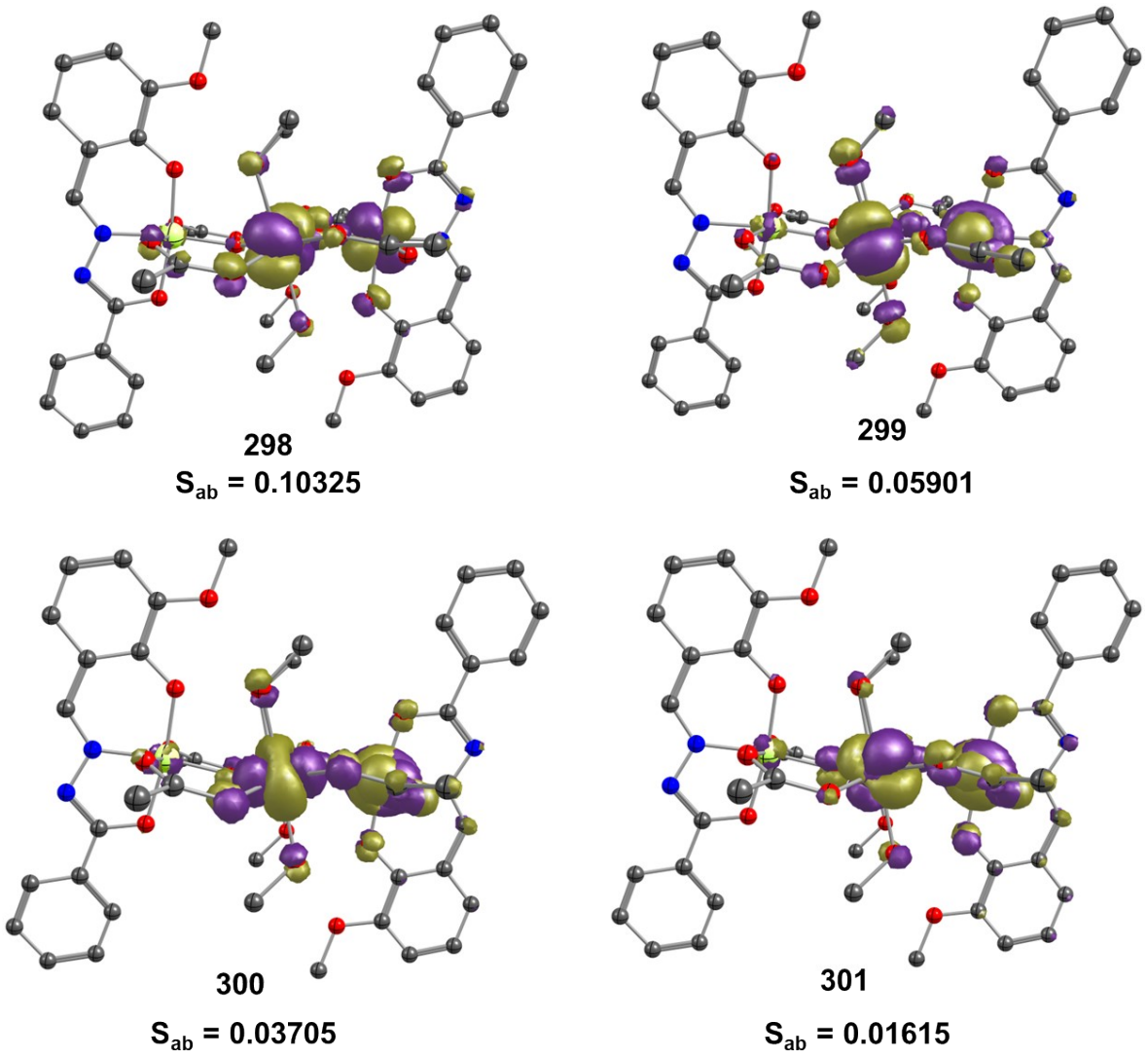

Figure S25. DFT computed corresponding orbitals for which the overlap integral values were calculated for $\mathbf{1_b}$ equivalent to J_{wb1} interaction of complex **1** at contour value = 0.07 e - /bohr^3.

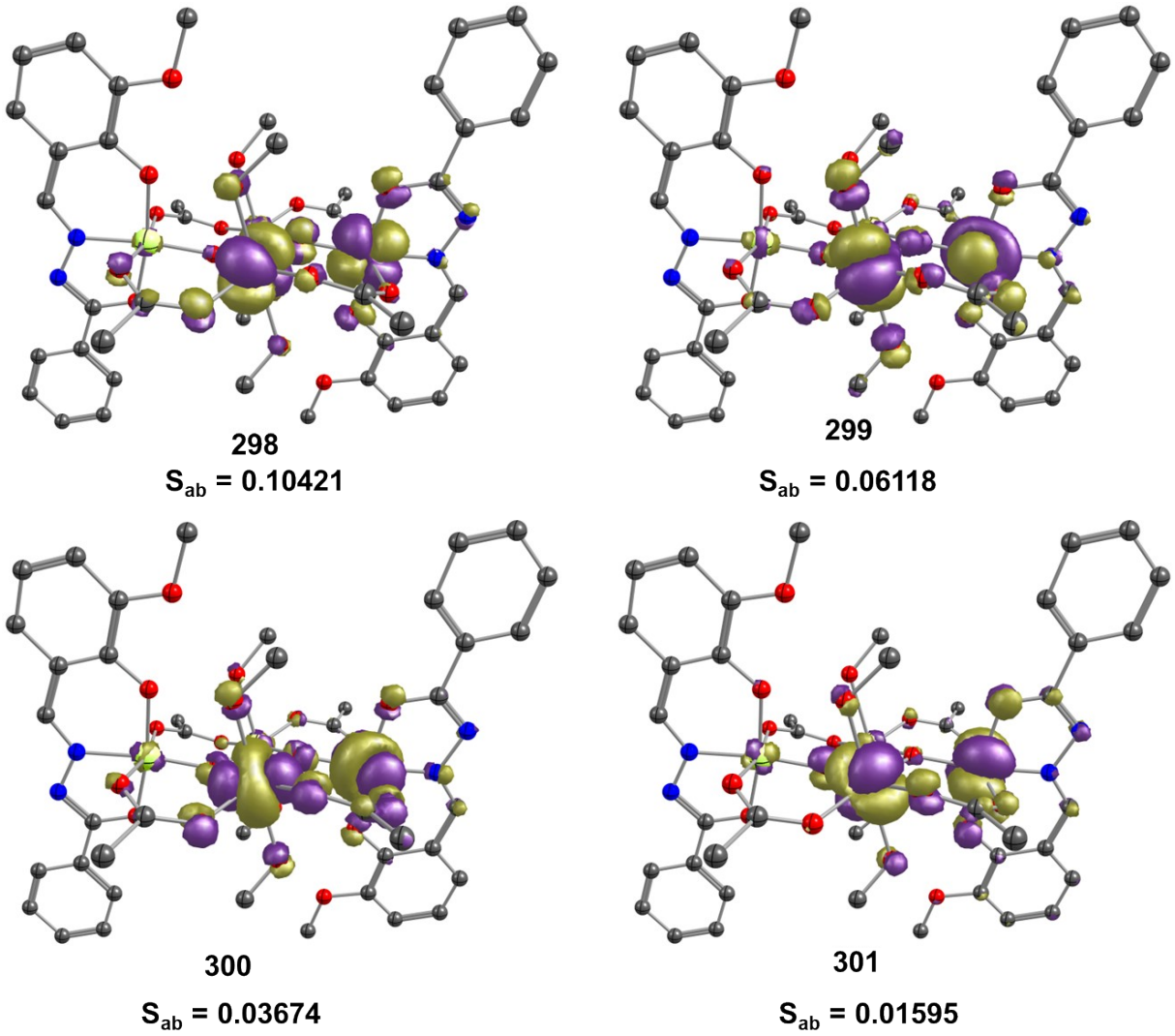

Figure S26. DFT computed corresponding orbitals for which the overlap integral values were calculated for $\mathbf{1_c}$ equivalent to J_{bb} interaction of complex **1** at contour value = 0.07 e^- /bohr^3.

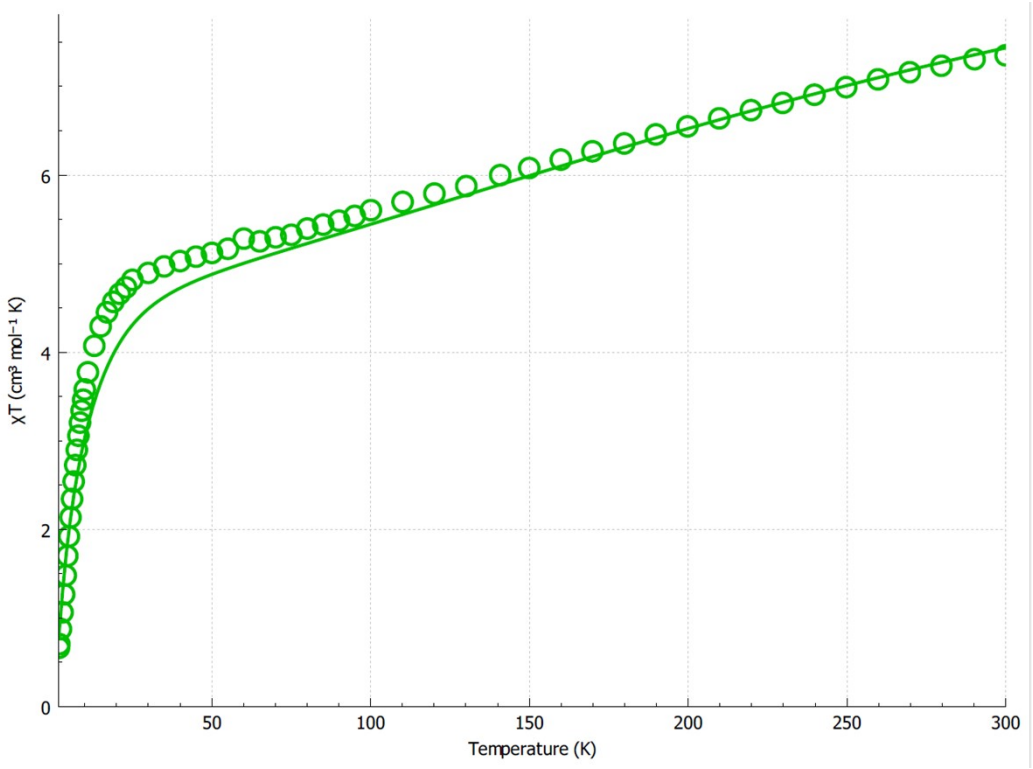

Figure S27. Temperature dependence of χT products for complex **1** under a DC field of 1000 Oe. The solid green lines represent simulated χT using the DFT *J* values.

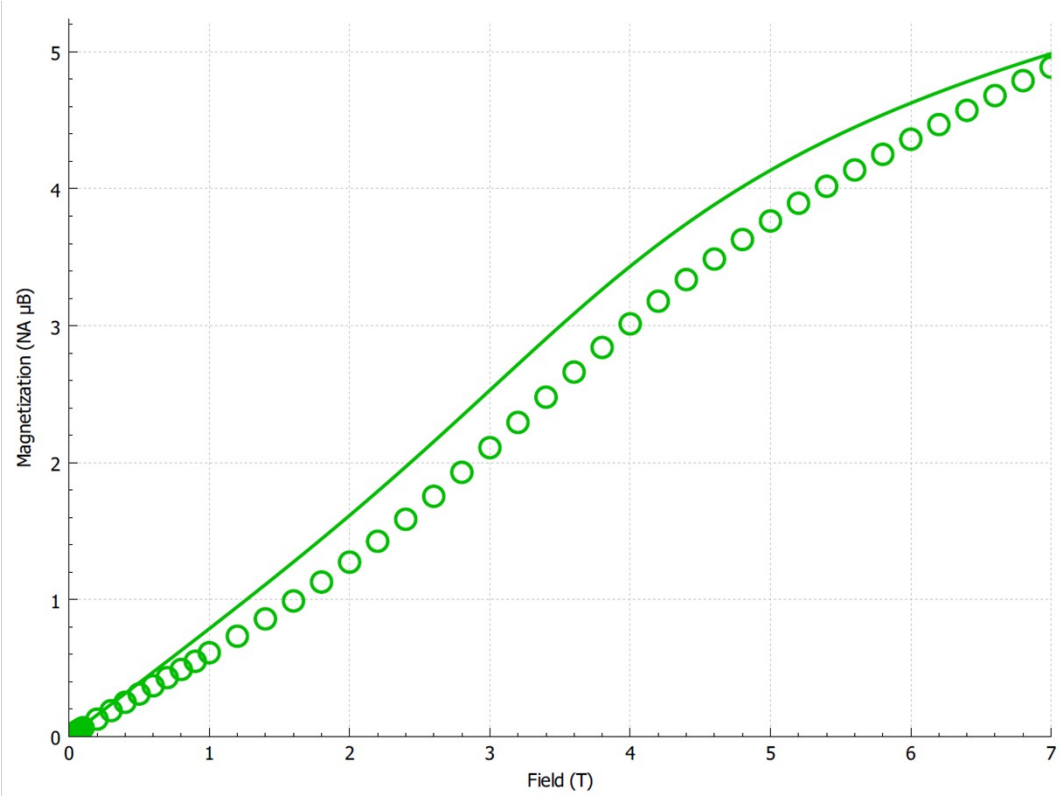

Figure S28. Field dependence of the magnetization data at 2 K for complex **1**. The solid green lines represent simulated magnetization using the DFT *J* values.

Table S13. BS-DFT computed energies of high-spin and broken-symmetry solution, spin densities, and *J* values complex **2**.

Solutions	Energy	ρ^{Mn1}	ρ^{Mn2}	$\langle S^2 \rangle$	J (cm^{-1})
HS	-4410.840358	3.75	3.75	20.0741	–0.43
BS	-4410.840421	3.74	-3.74	4.0598	

J values are estimated using the following equation,

$$\boldsymbol{J} = - \frac{E_{HS} - E_{BS}}{2S1\,S2 + S2}$$

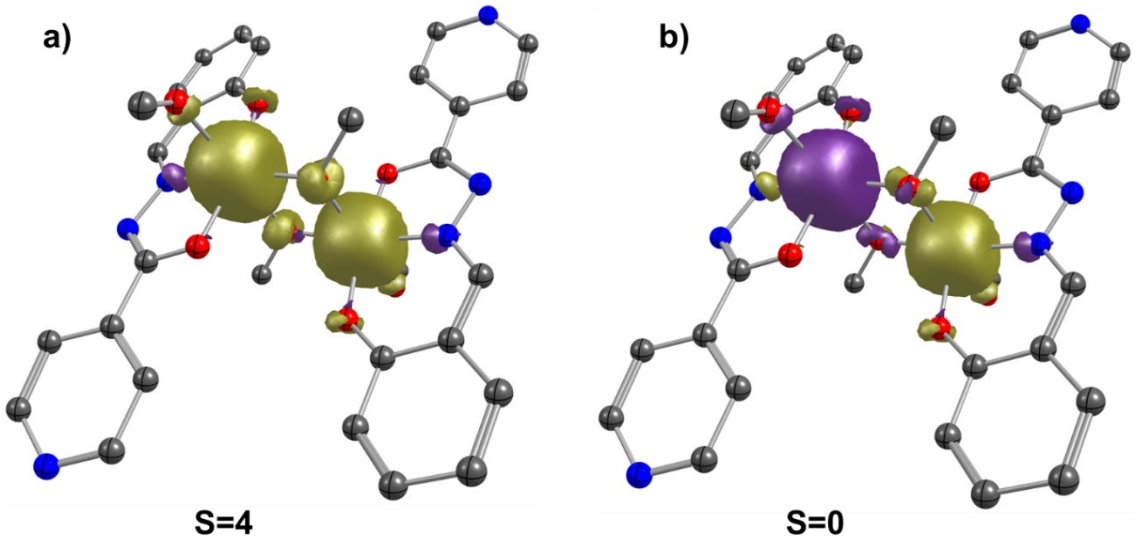

Figure S29. DFT computed spin-density plot of; (a) High Spin (S = 4); (b) Broken Symmetry (S = 0) of complex **2**. The olive green and purple color represents the positive and negative spin density respectively, with an isosurface value of 0.01 $e^-/bohr^3$.

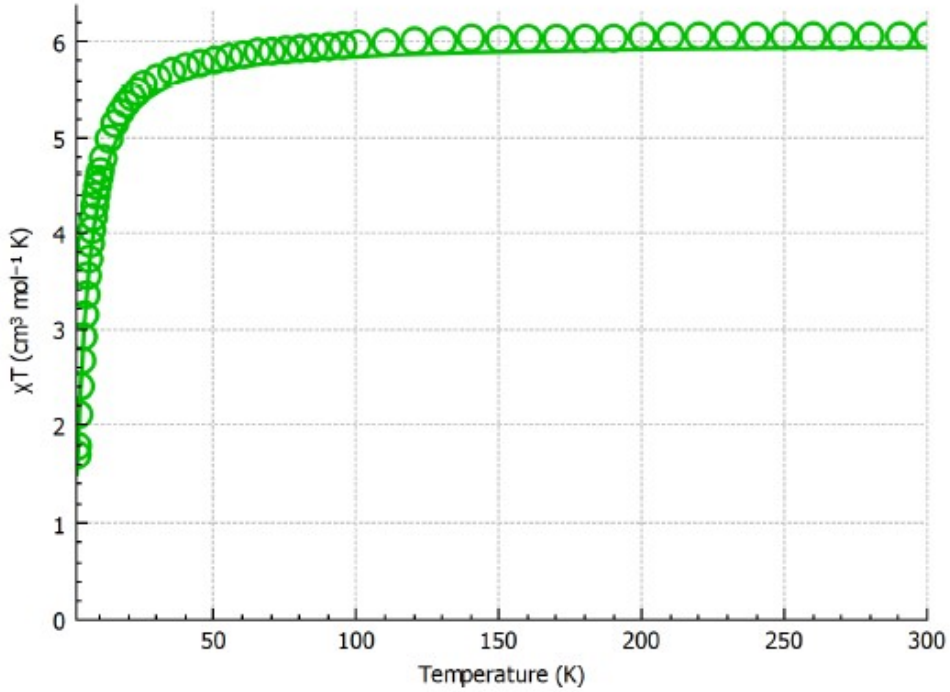

Figure S30. Temperature dependence of χT products for complex **2** under a DC field of 1000 Oe. The solid green lines represent simulated χT using the DFT *J* values.

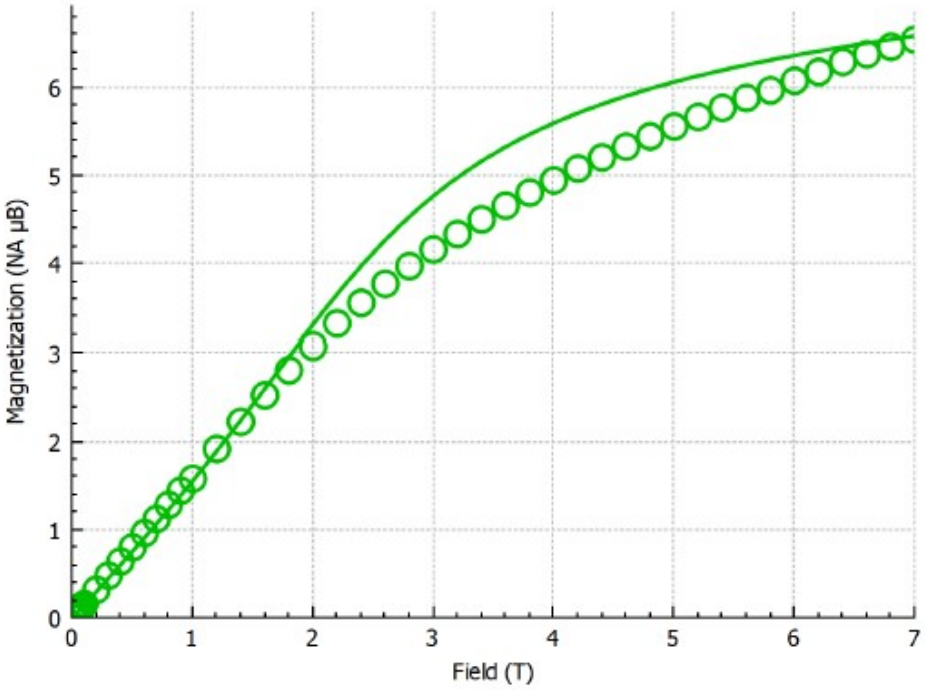

Figure S31. Field dependence of the magnetization data at 2 K for complex **2**. The solid green lines represent simulated magnetization data using the DFT *J* values.

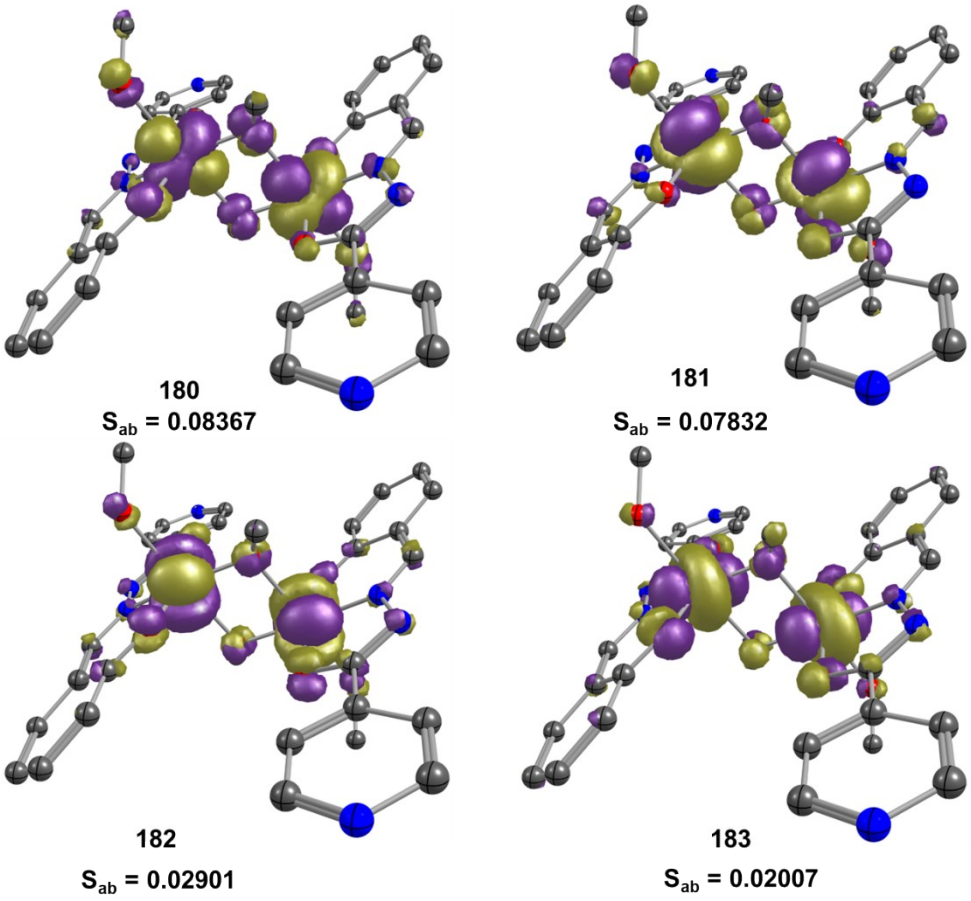

Figure S32. DFT computed corresponding orbitals for which the overlap integral values were calculated complex **2** at contour value = 0.07 e - /bohr^3.

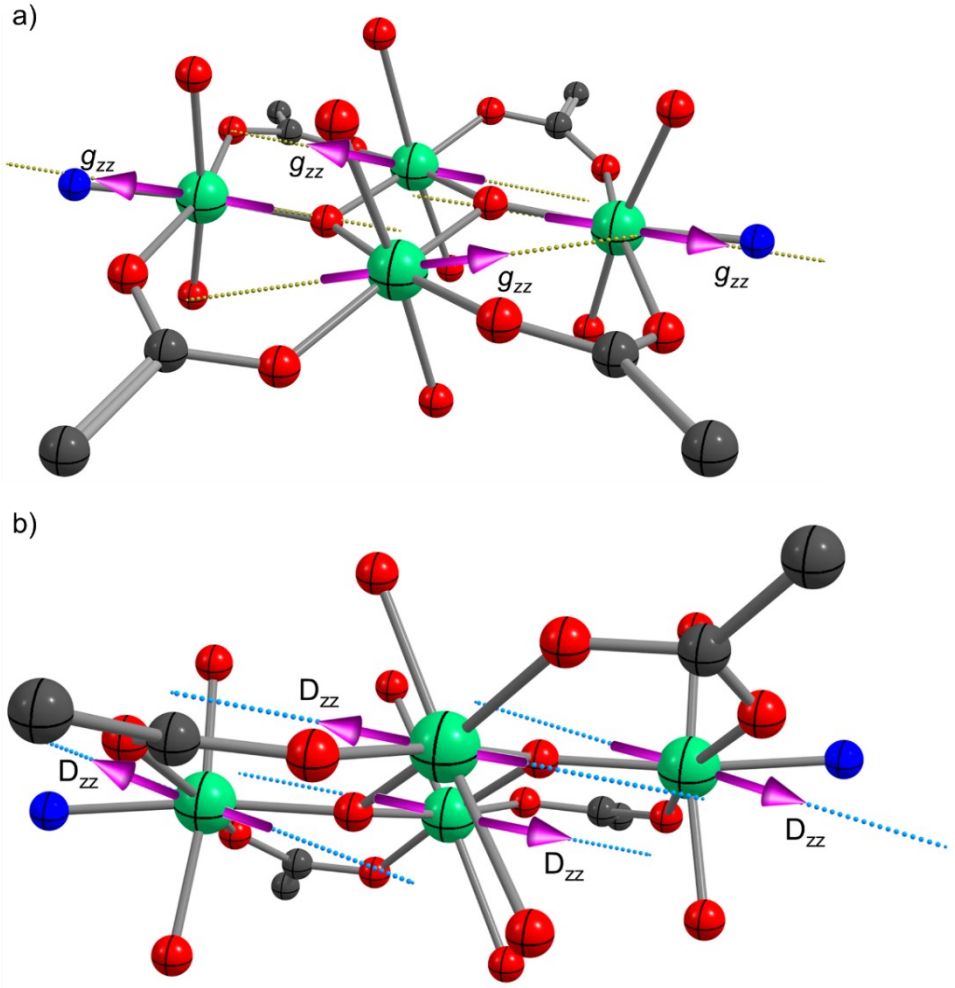

Figure S33. CASSCF computed the orientation of the (a) g-tensor and (b) D-tensor along the z-axis (main magnetic axis) for complex **1**.

Table S14. CASSCF (5,5) computed Spin–Hamiltonian parameter (g, D, |E/D|) parameters. All the D values are in cm^{-1}.

Parameters		**Monomers**	
		1′	**1″**
D	EHA	-3.26	-3.19
	PT2	-3.18	-3.11
|E/D|	EHA	0.08	0.00
	PT2	0.08	0.00
g_{xx}		1.970329	1.969296
g_{yy}		1.993416	1.99448
g_{zz}		1.996547	1.995082

EHA : Effective Hamiltonian approach ; 2PT : Second order perturbation Theory
1′ represents single-ion Mn(III) at wing position in complex **1**; **1″** represents single-ion Mn(III)

at body position in complex **1**

Table S15. Experimental and computed J and D values of complex **1**. All the values are reported here in cm^{-1}.

Parameters	Fitted using MAGPACK package	Calculated
D_w	-2.23	-3.26 (ab initio)
D_b	-2.09	-3.19 (ab initio)
J_{wb1}	-10.5	-7.6 (BS-DFT)
J_{wb2}	-6.9	-7.6 (BS-DFT)
J_{bb}	-26.6	-28.0 (BS-DFT)

Table S16. CASSCF computed 5 quintets (red) and 35 triplets (blue) states along with spin-orbit states for **1'** and **1''**. All the values are reported here in cm^{-1}

Monomers							
1′				**1″**			
Spin Free States	**Spin-Orbit States**			**Spin Free States**	**Spin-Orbit States**		
0.0	0.0	26683.9	40953.6	0.0	0.0	26741.9	42143.9
11972.4	0.1	26684.2	43181.0	13636.1	0.0	26751.8	42741.9
18814.1	9.1	26695.4	43203.7	18088.2	9.6	26871.1	42826.4
20717.8	10.6	26711.2	43231.0	19715.0	9.6	26876.4	42837.0
21240.6	13.2	26716.6	43835.9	20740.4	12.8	26879.9	43242.2
16352.8	11946.8	29678.3	43851.3	18581.5	13607.2	29952.4	43256.4
16924.7	11951.1	29679.6	43858.2	19244.5	13612.6	29955.1	43271.3
17999.9	11956.7	29681.4	47148.9	20224.5	13617.0	29957.9	45656.8
23113.6	11973.6	31968.4	47153.8	23280.5	13636.6	32511.8	45684.5
25386.8	11974.0	31977.5	47177.2	26016.9	13636.8	32533.5	45686.0
25944.1	16336.0	32008.6	47700.0	26326.1	18072.9	32534.2	46624.5
26644.4	16345.3	32098.8	47739.6	26621.1	18075.1	33682.5	46659.2
26663.8	16372.5	32139.1	47774.2	26848.9	18079.9	33707.7	46743.4
29652.7	16937.9	32146.2	48027.4	29933.0	18090.1	33739.4	46837.1
31984.0	16977.4	33489.5	48098.2	32515.4	18090.5	33764.6	46888.6
32066.1	16983.4	33498.1	48129.6	33691.5	18575.2	33811.1	46946.2
33461.3	18033.2	33502.0	48566.2	33733.1	18582.7	33812.5	48321.0
35277.1	18038.1	35264.2	48613.8	35315.4	18601.4	35332.9	48331.6
36275.6	18043.0	35276.5	48618.6	36118.2	19259.3	35339.3	48338.4
37490.3	18800.4	35288.8	48815.2	37026.8	19287.2	35347.2	48960.5
38676.9	18803.5	36289.5	48816.6	39388.4	19291.7	36126.5	48966.7
39973.6	18807.0	36305.3	48818.8	39925.9	19696.1	36138.9	48966.8
40081.1	18819.2	36317.2	50349.8	40046.7	19696.9	36145.0	49724.9
40301.8	18819.5	37506.7	50372.9	40439.3	19719.2	37041.6	49725.0
40544.9	20674.4	37519.8	50391.5	40581.1	19728.3	37047.4	49727.0
40862.1	20674.7	37522.1	50627.0	42125.7	19733.4	37056.7	50807.6
43179.4	20709.8	38683.3	50629.0	42747.8	20255.0	39391.1	50808.1
43790.3	20717.3	38707.0	50634.2	43175.0	20255.5	39402.8	50859.6
47157.2	20728.1	38707.5	50835.1	45686.2	20256.3	39404.3	51033.3
47738.9	21247.9	39952.1	50876.7	46681.9	20753.3	39842.2	51060.6

48050.0	21259.1	39956.7	50900.8	46793.5	20755.6	39851.1	51104.6
48528.0	21264.5	39990.3	51367.3	48280.9	20767.6	39900.8	51403.2
48779.0	21299.0	40039.5	51373.6	48932.9	20780.4	40058.4	51405.6
50394.3	21299.2	40055.4	51376.3	49692.9	20782.0	40126.4	51448.8
50594.5	23134.0	40125.4	51411.4	50832.1	23299.3	40133.5	51632.3
50800.7	23134.9	40312.5	51452.9	51057.9	23299.4	40411.3	51638.3
51334.4	23142.3	40326.7	51454.4	51400.2	23307.8	40450.3	51699.6
51377.7	25330.8	40364.3	54259.2	51545.7	25850.8	40517.0	53479.9
54216.8	25356.7	40604.5	54265.6	53435.5	25928.7	40651.2	53486.2
54814.0	25400.3	40643.0	54266.3	53809.8	25971.4	40686.5	53492.6
	25963.6	40666.3	54861.1		26320.0	40740.1	53851.5
	26061.6	40917.2	54862.7		26481.4	42093.4	53857.9
	26070.0	40920.3	54865.4		26482.6	42130.5	53863.8
	26679.5				26684.2		

9. Synthesis:

Synthesis of complex $[Mn_{10}(L^4)_8(OL^4)_2(DMF)_4(MeOH)_4(H_2O)_2]$ (**4**) was prepared by utilizing thiophene-2-carbonyl salicyl hydrazide (H_3L), which was made using salicylhydrazide and thiophene carbonyl chloride as given below.

Preparation of N-thiophenoylsalicylhydrazide (H_3L^4):

To prepare salicylhydrazide initially, 2.5 g of salicylic acid was taken in the mixture of 50 mL MeOH to which 4 mL Conc. HCl was added and refluxed for 24 h to get methylsalicylate. Then excess acid was neutralized by sodium bicarbonate solution and extracted in $CHCl_3$ and then solvent was removed under reduced pressure to get 2.0 g oily product. A mixture of (2.0 g; 13.15 mmol) methyl salicylate and corresponding hydrazine (1.25 equivalent, 16.437 mmol; 821 mg) was taken in 10 mL of EtOH and refluxed for 12 h to get white solid product. The product was isolated and recrystallized from hot ethanol. ^{1}H NMR (400 MHz, DMSO-d_6, δ ppm): 12.5, 10.02, (s, s; 2H, amide and phenolic OH), 8.13 (dd, 1H, phenyl proton), 7.35 (q, 1H, phenyl proton), 6.84 (p, 2H, phenyl proton), 4.52 (s, 2H, ring proton).

1.0 g of thiophene-2-carboxylic acid was dissolved in 5 mL of thionyl chloride and stirred for 1.5 h. After that, it was refluxed for 4 h and then the excess thionyl chloride was removed under

reduced pressure to obtain thiophene-2-carbonyl chloride (667 mg; 4.552 mmol). The thiophene-2-carbonyl chloride was dissolved in 15 mL of $CHCl_3$, to which triethyl amine (0.637 mL; 4.552 mmol) was added at 0 ºC and stirred for 5 minutes. Five minutes later, freshly prepared solid salicylhydrazide (4.552 mmol; 692 mg) was added slowly, followed by stirring at room temperature for one hour to get a white suspension which was further refluxed for 30 min. The product was isolated as a white solid upon cooling the mixture in the refrigerator. The amount of the product obtained was 480 mg. ^{1}H NMR (400 MHz, $CDCl_3$-d, ppm, δ): 11.45, 10.107, 10.02 (s, s, s; 3H, amides and phenolic OH), 7.403(dd, 2H, aromatic ring proton), 7.05 (s, 1H, ring proton), 6.83 (dd, 1H, ring proton), 6.574 (s,1H, ring proton) and 6.38 (dd,2H, ring proton). IR (KBr, cm^{-1}): 3202 (m), 3010(m), 2855(w), 1633(s), 1594(s), 1535(s), 1492(s), 1418(m), 1348(m), 1301(s), 1248(m), 1237(m), 1205(m), 1158(m), 1130(w), 1089(w), 1035(m), 940(w), 902(w), 844(m), 823(m), 748(s), 712(s), 664(m), 584(m), 536(s), 451(m).

Mass: TOF ES+ 261.0532 corresponding to mono deprotonated H_3L^4 species after a loss of H-atom.

Discussion:

The crystal structure of $[Mn_{10}(L^4)_8(OL^4)_2(DMF)_4(MeOH)_4(H_2O)_2]$ (**4**) reveals that two H_3L^4 ligands were oxidized (sulfoxidation) at the S-center of thiophene ring to produce corresponding thiophene-S-oxide (H_3L^4O) (Scheme S1). The Mn^{II} salt was reacted with H_3L^4 in a mixture of DMF and MeOH in an open atmosphere and in the presence of the ligand Mn^{II} is oxidized to Mn^{III} to form Mn^{III}_{10} (**4**) complex. The IR absorption peaks corresponding to S=O observed at 1000-1100 cm^{-1}; however, the region is also common for N-N single bond. Since ligand contains N-N single bond, thus it [1089(w), 1035(m) in H_3L^4 and 1089(w), 1032(m) in **4**] is not possible to assign unambiguously. The crystal structure shows thiophene S=O bond and because of which, thiophene ring lost its planarity, with the sulfur atom puckered

up from the plane of the four-ring carbon atoms, which has also been observed in [Cp*Rh(TMTO)] compound. The famous Jacobsen´s catalyst contains one Mn^{III} which was used for enantioselective epoxidation of olefins. Thus $\{Mn^{III}(L)\}$ moiety plausibly responsible for sulfoxidation leading to H_3L^4 to H_3L^4O. Thiophenes are completely unreactive towards oxygen in laboratory conditions. Thiophene is resistant to sulfoxidation since this will lead to distortion in the thiophene aromatic ring and partially hamper the aromaticity in thiophene-S-oxide. In the literature, several procedures were developed for converting thiophene into thiophene-S-oxide. The most commonly used reagents are either metachloroperbenzoic acid (mCPBA) or hydrogenperoxide (H_2O_2) and because of the above reason, the yield is low. In the literature MnO_2 was used for this purpose. There is one report where Mn^{III} complex was used to oxidize non aromatic S-atom of diphenyl sulfide. However, recently oxidation of dialkyl sulfides to sulfoxides were achieved by catalytic amount TEMPO organic ligand in the presence of $Co(NO_3)_2$ and $Mn(NO_3)_2$ in acetic acid solution at little elevated temperature. Thus, our one is the first report to observe *in situ* sulfoxidation of 2-substituted thiophene into its corresponding thiophene-S-oxide using Mn^{III} sources.

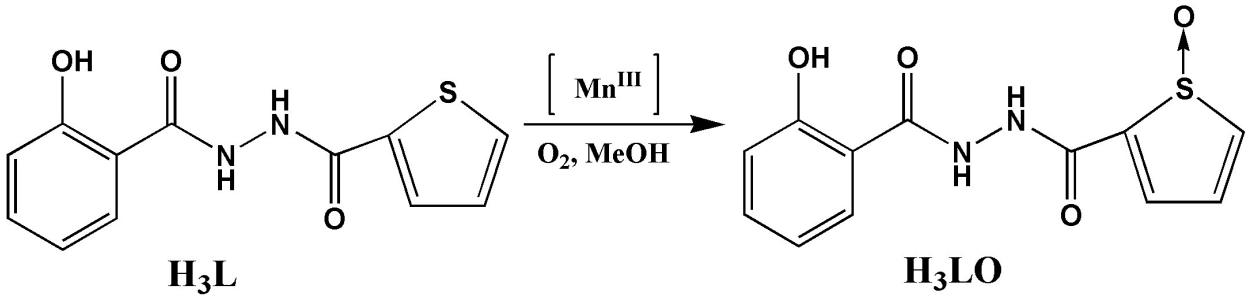

Scheme S1. The oxidation of N-thiophenoylsalicylhydrazide (H_3L^4) to thiophene-S-oxide (H_3L^4O).

10. Powder XRD pattern of pyrolyzed products (manganese-oxide)

Complexes **1**-**4** are subjected to pyrolysis at 800 °C for 3 h continuously in open air. At the end of 3 h, the corresponding black oxides products were allowed to cool down to room temperature. Then, the obtained black powder was subjected to powder X-ray diffraction analysis at room temperature in the range corresponding to 5 to 90°. The recorded powder pattern well matches with the pure cubic phase of α-Mn_2O_3 (JCPDS no. 41-1442) corresponding to the *I*a3 space group.[3] Therefore, a Powder X-ray diffraction study indicating all four complexes finally decomposed at very high temperatures to leave the Mn_2O_3 residue finally.

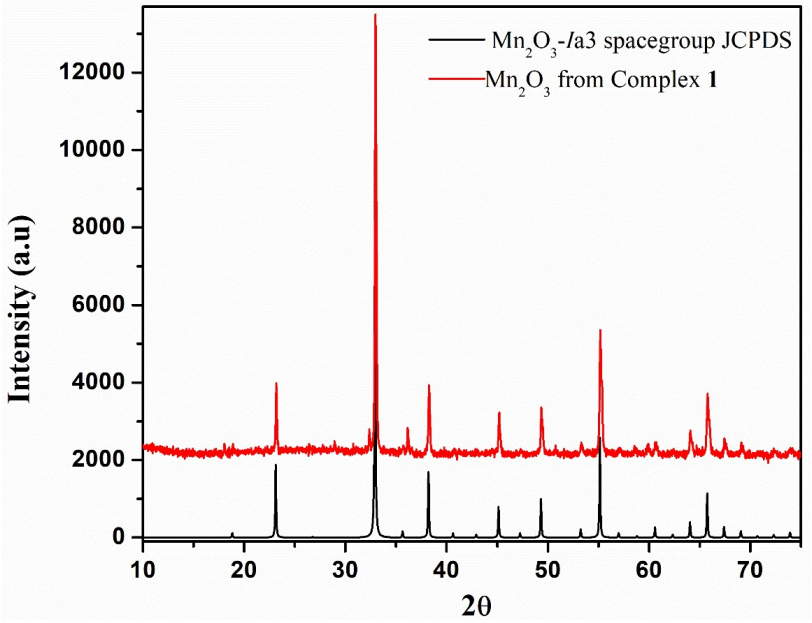

Figure S14. Overlay of powder pattern of Mn_2O_3 obtained upon the pyrolysis on **1** in open air and JCPDS card of Mn_2O_3 with *I*a3 space group.

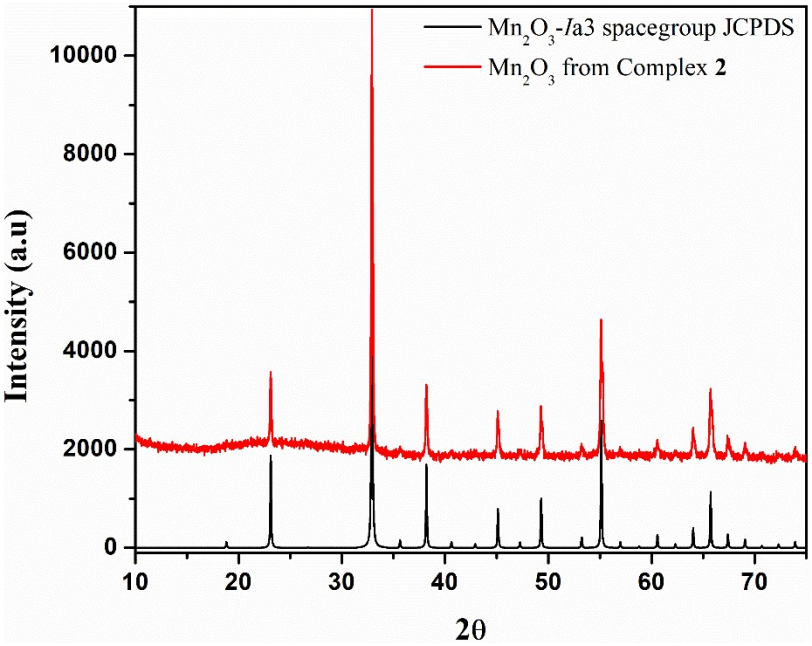

Figure S15. Overlay of powder pattern of Mn_2O_3 obtained upon the pyrolysis on **2** in open air and JCPDS card of Mn_2O_3 with *I*a3 space group.

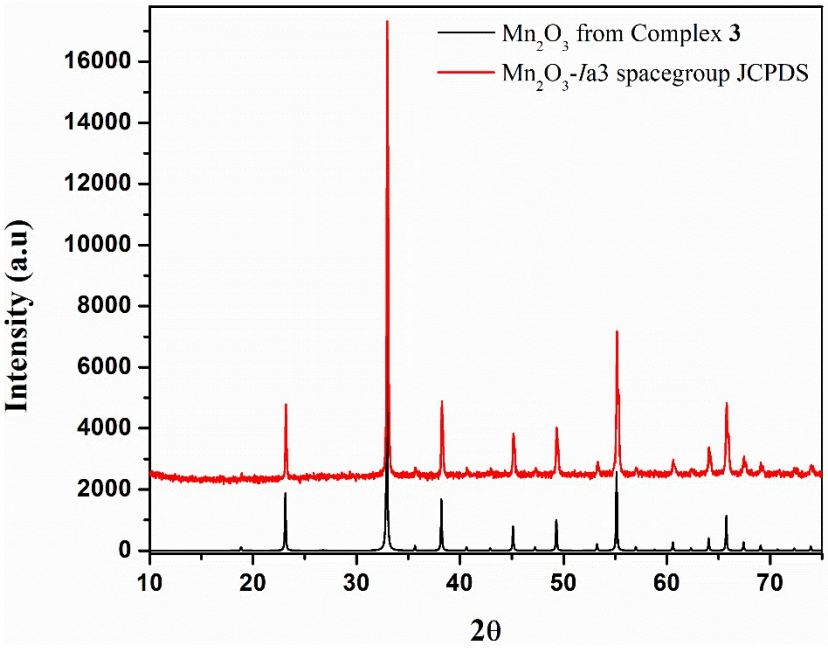

Figure S16. Overlay of powder pattern of Mn_2O_3 obtained upon the pyrolysis on **3** in open air and JCPDS card of Mn_2O_3 with *I*a3 space group.

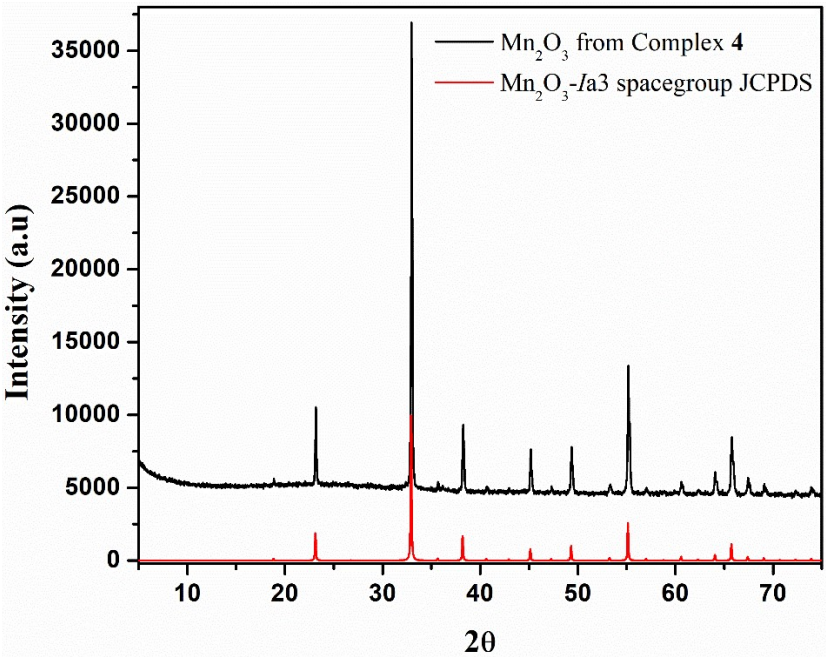

Figure S17. Overlay of Powder pattern of Mn_2O_3 obtained upon the pyrolysis on **4** in open air and JCPDS card of Mn_2O_3 with *I*a3 space group.

11. References

1. A. Trzesowska, R. Kruszynski and T. J. Bartczak, New lanthanide–nitrogen bond-valence parameters. *Acta. Cryst*. 2005, **61**, 429-434.

2. O. C. Gagné and F. C.; Hawthorne, Comprehensive derivation of bond-valence parameters for ion pairs involving oxygen. *Acta. Cryst*. 2015, **7***,* 562-578.

3. T. Z. Ren, Z.Y. Yuan, G. H. Du, and B. L. Su, in *Studies in surface science and catalysis*, Elsevier, 2006, **162**, 425-432. (doi:10.1016/s0167-2991(06)80936-5).